Nano-Structures & Nano-Objects 18 (2019) 100314

Contents lists available at ScienceDirect

Nano-Structures & Nano-Objects

journal homepage: www.elsevier.com/locate/nanoso

Titanium dioxide/agglomerated-free reduced graphene oxide hybrid photoanode film for dye-sensitized solar cells photovoltaic performance improvement

A.B. Suriani [a,b,*], Muqoyyanah [a,b], A. Mohamed [c], M.H. Mamat [d], M.H.D. Othman [e], M.K. Ahmad [f], H.P.S. Abdul Khalil [g], P. Marwoto [h], M.D. Birowosuto [i]

[a] Nanotechnology Research Centre, Faculty of Science and Mathematics, Universiti Pendidikan Sultan Idris, 35900 Tanjung Malim, Perak, Malaysia
[b] Department of Physics, Faculty of Science and Mathematics, Universiti Pendidikan Sultan Idris, 35900 Tanjung Malim, Perak, Malaysia
[c] Department of Chemistry, Faculty of Science and Mathematics, Universiti Pendidikan Sultan Idris, 35900 Tanjung Malim, Perak, Malaysia
[d] NANO-ElecTronic Centre (NET), Faculty of Electrical Engineering, Universiti Teknologi MARA (UiTM), 40450 Shah Alam, Selangor, Malaysia
[e] Advanced Membrane Technology Research Centre, (AMTEC), Universiti Teknologi Malaysia, 81310 Skudai, Johor, Malaysia
[f] Microelectronic and Nanotechnology–Shamsuddin Research Centre (MiNT-SRC), Faculty of Electrical and Electronic Engineering, Universiti Tun Hussein Onn Malaysia, 86400 Parit Raja, Batu Pahat, Johor, Malaysia
[g] Wood, Paper and Coating Division, School of Industrial Technology, Universiti Sains Malaysia, 11800 Pulau Pinang, Malaysia
[h] Materials Research Group, Thin Film Laboratory, Faculty of Mathematics and Natural Science, Universitas Negeri Semarang (UNNES), 50229 Sekaran Gunungpati, Semarang, Indonesia
[i] CNRS International Nanyang Technological University Thales Research Alliance (CINTRA), Research Techno Plaza, 50 Nanyang Drive, Border X Block, 637553, Singapore

HIGHLIGHTS

- Improved DSSCs photovoltaic performance was achieved by using annealed photoanode film.
- Enhanced DSSCs photovoltaic performance was obtained by hybridizing an annealed photoanode film with the custom-made hyper-branched TC14-rGO.
- Improved DSSCs photovoltaic performance was achieved by different photoanode configuration.
- The hybridization of TC14-rGO with MWCNTs increased the electrical performance of CE thin film.

GRAPHICAL ABSTRACT

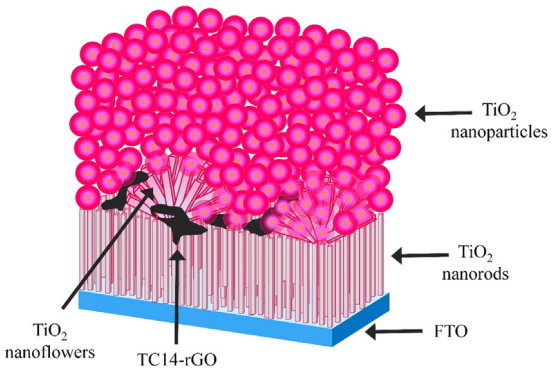

ARTICLE INFO

Article history:
Received 5 November 2018
Received in revised form 12 March 2019
Accepted 16 April 2019

Keywords:
rGO
Hyper-branched surfactant
MWCNTs
Hybid photoanode
DSSCs

ABSTRACT

In this work, the role of agglomerated-free reduced graphene oxide (rGO) in the modification of titanium dioxide (TiO_2) photoanode film was investigated for the enhancement of photovoltaic performance in dye-sensitized solar cells (DSSCs). The rutile TiO_2 nanorods–nanoflowers (NRs–NFs) and the photoanode layer consisting of anatase TiO_2 nanoparticles (NPs) were synthesized by the simple hydrothermal growth and squeegee method, respectively. Post-annealing treatment of TiO_2 NRs–NFs was also done in order to investigate its effect on the DSSCs performance. Meanwhile, the rGO solution was produced by reducing a graphene oxide (GO) solution utilizing hydrazine hydrate via a chemical reduction process. The initial GO solution was synthesized by electrochemical exfoliation assisted by a hyper-branched sodium 1,4-bis (neopentyloxy)-3-(neopentyloxycarbonyl)-1,4-dioxobutane-2-sulphonate (TC14) surfactant. The produced TC14-rGO was also hybridized with multi-walled

* Corresponding author at: Department of Physics, Faculty of Science and Mathematics, Universiti Pendidikan Sultan Idris, 35900 Tanjung Malim, Perak, Malaysia.
E-mail address: absuriani@yahoo.com (A.B. Suriani).

https://doi.org/10.1016/j.nanoso.2019.100314

carbon nanotubes (MWCNTs), which then coated by thin platinum (Pt) NPs (TC14-rGO_MWCNTs/Pt) and used as counter electrode (CE) thin film. Based on solar simulator measurements, the highest energy conversion efficiency (η) (1.559%) was achieved by TiO_2 NRs–NFs/TC14-rGO/TiO_2 NPs hybrid photoanode film with the short current density (J_{sc}), open circuit voltage (V_{oc}), and fill factor (FF) of 3.275 mA/cm^2, 0.747 V, and 53.5, respectively as compared to others fabricated photoanode films; non-ann TiO_2 NRs–NFs/TiO_2 NPs (1.215%), ann TiO_2 NRs–NFs/TiO_2 NPs (1.462%), and TiO_2 NRs–NFs/TiO_2 NPs/TC14-rGO (0.525%). This result shows that the utilization of TC14-rGO for both photoanode and CE film increases the conductivity of the film. High η was also supported by high dye adsorption promoted by TiO_2 NPs as the top photoanode layer.

1. Introduction

The development of solar cell technology has gained a lot of interest since the invention of first-generation silicon wafers solar cells in the 20th century by Russell Ohl and the next second-generation solar cells based on amorphous silicon, copper indium gallium selenide (CIGS), and cadmium telluride (CdTe). Good performance and high efficiency (η) of around ∼20% was recently achieved and became a potential candidate for reducing and slowly replacing the usage of fossil fuel as an energy source [1]. However, the scarcity of source elements, high vacuum processes, and high-temperature treatment induced high production costs, thereby limiting the fabrication of such solar cells at industrial scales [2]. The dye-sensitized solar cells (DSSCs) as the third-generation solar cell was first invented by O'Regan and Grätzel in 1991 [3] and became a promising candidate to overcome problems for the current generation. DSSCs offers a simple fabrication, flexibility and design opportunities, low-cost material, light weight, and relatively high η [3–6]. Recently, 14% efficiency was achieved [7] and presents a possibility to match the capabilities of CIGS and CdTe solar cells. In order to increase DSSCs performance, several improvements on four main DSSCs components were widely investigated. These components include the photoanode, dye, electrolyte, and counter electrode (CE).

Among the four components, the photoanode, which is commonly fabricated from semiconductor materials, is crucial for the improvement of DSSCs efficiency due to its role on providing the surface area for the adsorption of dye molecules, light absorption, and also transferring excited electrons to the substrate. Zinc oxide (ZnO) [8] and titanium dioxide (TiO_2) [9–11] were the most popular semiconductor materials investigated in the DSSCs application. This was due to their nontoxicity, wide band gap energy (needed for light absorption), and good carrier mobility. ZnO presents better carrier mobility, lower electron recombination, and a flexible synthesis process as compared to TiO_2 [12]. Recently, a high DSSCs η of 8.22% was achieved when ZnO was treated by a 1H,1H,2H,2H-perfluorodecyltriethoxysilane (PFDTES) hexane solution after dye immersion [13]. However, the smaller chemical stability of ZnO yields the precipitation after dye immersion; this resulted in less dye loading, poor electron injection, and lower efficiency [12,14]. TiO_2 offers better chemical and physical stabilities, large surface area, and presents a higher DSSC efficiency as compared to ZnO thus suitable to be applied as a photoanode material [14–16]. TiO_2 has three crystallite forms (phases), which are commonly known as anatase, rutile, and brookite. Brookite was not beneficial for several applications due to its unstable form at room temperature. Anatase is a metastable phase that can transform into rutile by high temperature, while rutile is the most stable form. Both anatase and rutile phases were commonly utilized for DSSCs applications due to their high photocatalytic activity [17]. However, the drawback of TiO_2 as compared to ZnO as photoanode is its lower electron mobility and higher electron recombination, thus requiring improvement [12].

It is known that TiO_2 morphology can critically affect the DSSCs performance, thereby its improvement and modification were widely investigated to solve this problem [18]. Several TiO_2 morphologies which had been successfully synthesized and applied as photoanodes were nanoparticles (NPs) [19], nanorods (NRs) [16,20], nanowires (NWs) [21], nanotubes [22], nanoflowers (NFs) [23], and hollow hemispheres [24]. Meanwhile, usual synthesis methods for TiO_2 were sol–gel, chemical vapor deposition (CVD), solvothermal, and hydrothermal growth methods. Among those methods, hydrothermal growth is simple, low-cost, fast reaction velocity, and has the necessary flexibility for controlling the TiO_2morphology. The zero-dimensional (0D) TiO_2 NPs provide a large specific area for effective dye adsorption, which may increase DSSCs efficiency [25,26]. On the other hand, one dimensional (1D) TiO_2 nanostructures, such as NRs and NWs, offer faster and direct electron pathways to the substrate due to their vertically aligned morphology [27–29]. The combination of both morphologies and phases was proven to give better DSSCs performance as compared to the pure phase. Hafez et al. [30] show that pure TiO_2 NRs and TiO_2 NPs give lower η (4.4 and 5.8%, respectively) as compared to the TiO_2 NRs/NPs bilayer (7.1%). Cao et al. [26] also achieved a higher η of 7.39% by utilizing a bilayered photoanode consisting of TiO_2 NRs and NPs as compared to pure film (0.54 and 4.63% for NRs and NPs, respectively). This result was also in a good agreement with several works done by utilizing both different morphologies and phases of NRs and NPs [25,31,32].

Post-treatment of TiO_2 nanostructures, such as annealing, also critically affects the optical and electrical properties of fabricated films. Ahn et al. [33] show that post-annealing of TiO_2 nanobarbed fibers resulted in higher crystallinity and higher conductivity as indicated by a lower band gap energy (E_g). Hasan et al. [34] reported that the TiO_2 morphology structure remains unchanged as the annealing temperature increases (300−600 °C), while its transmittance decreases due to surface roughness. Meanwhile, Zhao et al. [35] showed that the surface roughness factor for TiO_2 NPs increases with the annealing temperature (350−600 °C). A low annealing temperature (350 °C) yields small-sized crystallites, while a higher temperature (600 °C) improves the crystallinity, thus decreasing the internal surface area and impending the dye adsorption. Moreover, Meng et al. [36] found that the top ends of TiO_2 NRs sharpen as the annealing temperature increases (200−500 °C). They also showed that higher DSSCs η is achieved by the annealed films as compared to the as-deposited films without annealing. This is also in a good agreement with results from Ahmad et al. [20], who obtained the highest dye adsorption and DSSCs η by annealing TiO_2 NRs at 450 °C for 30 min.

Besides post-annealing treatment, the hybridization of TiO_2 nanostructures with carbonaceous material, such as carbon nanotubes (CNTs), graphene, graphene oxide (GO), or reduced GO (rGO) was also done in order to improve TiO_2 electrical properties [11,37–44]. This was due to the high conductivity of the carbonaceous material, which increases the electron transfer through TiO_2, decreases the electron recombination, and yields

higher short circuit current density (J_{sc}). Among these carbonaceous material, rGO offers an advantage for the functionalization and hybridization with other material due to the presence of oxygen-functional groups resulted from the reduction process of GO [45]. This oxygen-functional groups can form a strong-coupling composite between the rGO and TiO_2 [46]. A higher η of 7.52% was achieved by Zhao et al. [43] with a TiO_2-rGO nanocomposite via a one-step hydrothermal method as compared to a pure film of TiO_2NPs (6.39%). Meanwhile, Liu et al. [40] achieved 6.85% efficiency when immersing the prepared TiO_2NPs in the GO solution and then reducing them via thermal reduction process. However, they also found that less dye adsorption occurred in the sample with excess rGO. This leads to the conclusion that a high amount of rGO must be avoided. The configuration of the photoanode film also gives different effects in DSSCs performance. Song et al. [41] sprayed a rGO layer on TiO_2 NPs and achieved 6.06% efficiency. They also found that a thicker rGO layer was not beneficial for dye adsorption, which decreased η. In contrast, Liu et al. [42] deposited the rGO layer between TiO_2 NPs films by the electrospray method. By spraying 1 layer of rGO (40 nm) between two TiO_2 NPs films, a higher efficiency (7.8%) was obtained as compared to pure TiO_2 NPs films (7.1%) and thicker (120 nm) rGO layers (7.3%). Furthermore, when they investigated multiple rGO layers between the TiO_2 NPs films, the highest η (8.9%) was achieved by three rGO layers as compared to five layers rGO (6.1%).

However, most reported papers used the GO or rGO powder synthesized through Hummers method which well-known using the highly toxic chemicals and more complex synthesis steps [40,43,47]. The challenge and more step (dissolving in solvent) on the thin film fabrication method due to the powder form of the synthesized GO can be minimized by developing new GO synthesis method. The simple and water-based GO synthesized by using electrochemical exfoliation becomes a promising solution to minimize these drawbacks which can further easily fabricated by spraying method. In this work, the novel hybridization of TiO_2 NRs–NFs synthesized by hydrothermal growth with rGO based on hyper-branched sodium 1,4-bis (neopentyloxy)-3-(neopentyloxycarbonyl)-1,4-dioxobutane-2-sulphonate (TC14) surfactant produced by chemical reduction was done by simple spray deposition before applying TiO_2 NPs by the squeegee method [19]. In addition, the post-annealing treatment of TiO_2 NRs–NFs after hydrothermal growth was also done in order to investigate its effect in DSSCs performance. The comparison summary between the recent literature of modified photoanode with this work are presented in Table 1.

CE also plays a key role in DSSCs performance to facilitate electron transfer which needed to regenerate the oxidized dye after electron excitation. Highly conductive materials such as platinum (Pt), multi-walled CNTs (MWCNTs), rGO, or a hybridization thereof become popular choices to be used as CEs [6,48]. Several works have already proven that a hybrid material poses better electrical properties as compared to a pristine CE film [6,48–51]. In this work, the resultant material from the hybridization of rGO, MWCNTs, and Pt NPs was utilized as the CE based on its highest performance, which was reported previously as compared to commercially available SDS surfactant [51]. The TC14-rGO was synthesized utilizing hyper-branched TC14 surfactant, which has been proven in previous reports to give better DSSCs performance by utilizing ZnO- and TiO_2 NWs-based photoanodes [14–16,51]. Meanwhile, the MWCNTs was synthesized from waste cooking palm oil as the carbon source [52,53]. The combination of both hybrid photoanode and CE materials was believed to give better DSSCs performance due to better crystallinity and electrical properties of the photoanode film and the high conductivity of CE thin film.

2. Material & methods

2.1. Fabrication of photoanode film

In this study, four types of fabricated photoanode films are non-annealed (non-ann) TiO_2 NRs–NFs/TiO_2 NPs, ann TiO_2 NRs–NFs/TiO_2 NPs, TiO_2 NRs–NFs/TiO_2 NPs/TC14-rGO, and TiO_2 NRs–NFs/TC14-rGO/TiO_2 NPs as illustrated in Fig. 1. Two photoanodes were without TC14-rGO and the two others were with TC14-rGO as different configurations of the photoanode film. In essence, all photoanode films consist of TiO_2 NRs–NFs and TiO_2 NPs. The rutile TiO_2 NRs–NFs were synthesized by the hydrothermal growth method as described in previous work [16] and used as the bottom layer of all fabricated photoanode films. In brief, the same volume ratio of deionized (DI) water and hydrochloric acid (HCl) were well mixed under constant stirring for 5 min. Afterward, titanium butoxide (TBOT) was added to the solution with the volume ratio of 1:40 and stirred for another 10 min until a clear solution was formed. Fluorine-doped tin oxide (FTO) was initially placed in the autoclave with the conducting surface facing upward before pouring the hydrothermal solution and then performing the hydrothermal growth for 5 h at 150 °C. After the autoclave was cooled down to room temperature, the synthesized TiO_2 NRs–NFs film was taken out and rinsed with DI water. The films were then dried at room temperature; some of them were annealed at 450 °C for 30 min as the post-treatment [20]. Meanwhile, the anatase TiO_2 NPs were prepared by mixing ethanol, titanium (IV) isopropoxide (TTIP), and titanium (IV) oxide in paste form and applied by the squeegee method [19]. The coated films were then heated for 10 min at 150 °C before being annealed at 450 °C for 1 h. The hybrid photoanode films were fabricated by spraying the TC14-rGO solution using the spray deposition method with an airbrush (0.3 mm nozzle diameter). The spraying process was performed at 10 cm distance from the preheated fabricated TiO_2 nanostructures film (120 °C for 5 min). The fresh sprayed films was then annealed at 400 °C for 1 h under argon atmosphere.

2.2. Fabrication of CE thin films

The fabrication of the TC14-rGO_MWCNTs/Pt CE thin film was initially done by synthesizing TC14-GO as the initial solution before undergoing the chemical reduction process as mentioned in the previous work [14–16,51]. The electrochemical exfoliation method was performed by connecting two graphite rods 7 V DC power supply for 24 h [14,15,51]. The rods were partially immersed in the water-based 0.1 M electrolyte solution containing custom-made hyper-branched TC14 surfactant. Afterward, a small amount of hydrazine hydrate was dropped to the synthesized GO and stirred for 24 h under ∼95 °C temperature to produce the TC14-rGO solution. One weight per cent of MWCNTs was further dispersed to the TC14-rGO solution and spray coated on the FTO substrate. In brief, the TC14-rGO_MWCNTs hybrid solution was sprayed on the preheated FTO (120 °C for 5 min) which then annealed at 400 °C for 1 h in an argon atmosphere [51]. The last step was sputter coating the 10 nm Pt NPs layer onto the CE film.

2.3. Fabrication of DSSCs

The DSSCs device was fabricated by assembling the dyed photoanode (non-ann and ann TiO_2 NRs–NFs/TiO_2 NPs, TiO_2 NRs–NFs/TiO_2 NPs/TC14-rGO, and TiO_2 NRs–NFs/TC14-rGO/TiO_2 NPs) and TC14-rGO_MWCNTs/Pt CE film followed by an electrolyte (1,2-dimethyl-3-propylimidazolium iodide (DMPII)) injection between them. Ruthenium (N719) was used as the dye, which

Table 1
The comparison summary between the recent literature of modified photoanode with this work.

TiO_2 nanostructures	Photoanode films	DSSCs η (%)	Reference
rGO-TiO_2 (anatase)	- The GO was synthesized by modified Hummers' method - The TiO_2 NPs film was immersed in the GO solution followed by sintering	TiO_2 NPs; 6.13 rGO-TiO_2 NPs; 6.85	[40]
TiO_2-rGO (anatase)	- The rGO was prepared by reducing the initial GO synthesized by modified Hummers' method - The TiO_2 NPs was sprayed by rGO solution with different time and configuration	TiO_2 NPs; 7.1 TiO_2 NPs/rGO/TiO_2 NPs; 7.8 TiO_2 NPs/rGO (3 layer of rGO between NPs); 8.9	[42]
rGO/TiO_2 (anatase–rutile)	- The rGO was prepared by reducing the initial GO synthesized by improved Hummers' method using ethylene glycol - The rGO/$TiO_2$was synthesized by hydrothermal method	TiO_2 NPs; 6.39 rGO-TiO_2 NPs; 7.52	[43]
rGO-TiO_2nanocomposite (anatase)	- The rGO was prepared by sonicating and stirring the initial GO synthesized by modified Hummers'-Offeman method - The rGO-$TiO_2$was fabricated by doctor blading method	TiO_2 NPs; 4.98 rGO-TiO_2 NPs; 7.68	[47]
TiO_2/rGO/TiO_2(anatase–rutile)	- The water-based rGO solution was prepared by reducing the initial GO synthesized by electrochemical exfoliation assisted by custom-made hyper-branched TC14 surfactant using hydrazine hydrate - The different configuration of photoanode film was fabricated by spraying the rGO solution on top and between the TiO_2 NRs–NFs and TiO_2 NPs	This work	

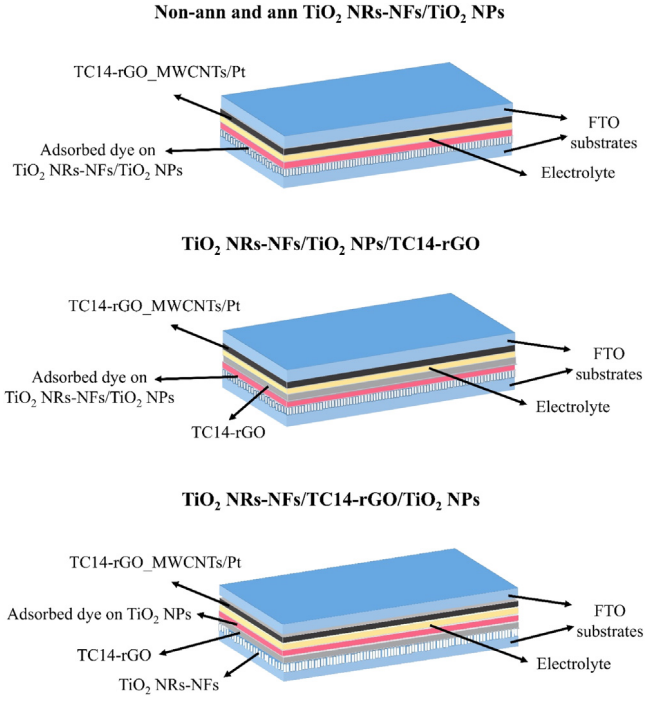

Fig. 1. Illustration of fabricated various photoanode films.

was initially prepared by dissolving it into a mixture of acetonitrile and 1-butanol in the same volume ratio. The photoanode immersion was fixed for 24 h followed by rinsing the dyed photoanode film with ethanol and dried at room temperature. Meanwhile, the redox couple of 1,2-dimethyl-3-propylimidazolium iodide (DMPII) was used as the electrolyte. The fabricated DSSCs were then measured by a solar simulator device in order to investigate their performance.

The morphological properties and their element compounds of fabricated photoanodes and CE thin films were investigated by a FESEM-Hitachi SU8020 and EDX-Horiba EMAX, respectively. The FESEM images were taken at working distance of 8 mm using upper detector with 5 kV accelerating voltage. Meanwhile, the EDX analysis were performed by using 30 kV accelerating voltage and 15 mm working distance. Furthermore, the structural properties were analyzed by a HRTEM-JEOL JEM 2100, XRD-Bruker D8 Advance, and a Renishaw InVia microRaman System for Raman spectroscopy. The HRTEM samples preparation was done by dispersing some drops of TC14-rGO solution in ethanol as solvent. The dispersed solution then sonicated for 5 min and 1–2 drops of solution was dropped on lacey carbon film (LC300-Cu on 300 mesh copper grids) followed by drying at room temperature. The analysis was done by performing 160 kV accelerating voltage. The electrical and optical properties comprised the electrical resistivity, transmittance, and band gap energy (E_g); they were measured by a Agilent Technologies Cary 60 UV–Vis and four-point probes instrument; a Keithley 2636A was the source meter and Leios TMXpert software was used for data analysis. DSSC photovoltaic performance was finally measured by solar simulator Oriel Sol 1A under 1AM solar illumination.

3. Results and discussion

3.1. FESEM, EDX, and HRTEM analysis

The top view morphology of synthesized TiO_2 NRs–NFs is presented in Fig. 2(a). Based on low magnification, the dense NRs without any holes or cracks were grown uniformly on the substrate. Higher magnification shows that the top TiO_2 facet has a tetragonal shape with smooth structure, in which the diameter ranges from 75.3 to 295 nm (Fig. 2(b)). This NR diameter range is consistent with observations from previous work [16] and confirms the reproducibility of the hydrothermal growth method for TiO_2 NRs–NFs. A cluster of NFs was clearly observed to be stacked on top of TiO_2 NRs; these NFs appear to have complete and incomplete structures (Fig. 2(c)). The complete single NF diameter is around 8.3 μm, while the two NFs colliding each other form a bigger NF with a diameter of 12.7 μm. Based on the incomplete NF structure, it can be concluded that the NFs were formed from one crystal nucleus, which had different crystal faces for growing NFs petals [54]. The FTO position during hydrothermal growth offers the place of the excess nucleating centers to "stay" thus formed the NFs [55]. The short hydrothermal synthesis time of 5 h prevents a potential glut of grown NFs, as proven by the observed rarity of NFs on NRs in the low magnification FESEM images. It can be seen in these images that the NFs had also formed with a tetragonal structure with a diameter slightly bigger than that of the tetragonal structure of NRs. This was believed to be due to the slow hydrolysis rate caused by the acidic solution, which offers the abundant Ti^{4+}as the source of TiO_2crystals. EDX analysis (Fig. 2(d)) shows the titanium (Ti) and oxygen (O) atomic

percentages of 27.03 and 72.97%, respectively which is consistent with the previous work [16].

The morphology of the tetragonal crystal structure of TiO_2 NRs was seen to remain unchanged after the annealing treatment. However, the top surface became rough as shown by blue arrows in Fig. 2(e), which is in good agreement with the results of several works [34,36,56,57]. The density and roughness of the ann film increased due to the deformation and recrystallization during the annealing treatment. The observed diameter of ann TiO_2 NRs was also slightly bigger in the range of 94−313 nm as compared to non-ann TiO_2 NRs. This resulted in reduced porosity for the film, which was proven by the lower amount of empty space between each NR. After TC14-rGO was sprayed on TiO_2 NRs–NFs, TC14-rGO layers were clearly observed to adhere to the NRs and NFs with the fold-up layer in the edge plane (Fig. 2(f)). The fold-up layer originates from the successful oxidation process during electrochemical exfoliation. In addition, the presence of the thin layer of TC14-rGO was due to the successful reduction process utilizing hydrazine hydrate as the reducing agent, which eliminates the oxygen-containing functional groups. The EDX analysis further confirmed Ti, O, and carbon (C) as the elemental components of the fabricated films (Fig. 2(g)). The inset shows that the C atomic percentage was slightly higher (44.51%) than O (42.24%), which is characteristic of the rGO sample due to its reduced O content after the chemical reduction process was carried out. However, the O atomic percentage in this sample was much higher as compared to the pristine TC14-rGO sample (∼66.66% of the result in previous work [16]) which was believed to be contributed by the O content of TiO_2 NRs–NFs.

The porous morphology of TiO_2 NPs comprising the top photoanode layer on non-ann and ann TiO_2 NRs–NFs/TiO_2 NPs films and also TiO_2 NRs–NFs/TC14-rGO/TiO_2 NPs hybrid photoanode films were seen to uniformly cover the entire bottom photoanode layer without any cracks (Fig. 2(h)). The NPs were interconnected closely to each other due to the effective TTIP molar ratio (0.1 M) used in the TiO_2 NPs paste preparation [19]. This also was supported by the second annealing of the TiO_2 NPs paste, which assisted the formation of particle interconnections, while the first annealing decomposed the residual organic compound [58]. The cross-section view of mixed-phase non-ann TiO_2 NRs–NFs/TiO_2 NPs shows that the fabricated photoanode film thickness was ∼17.35 μm and the TiO_2 NRs layer thickness was 3.38 μm (Fig. 2(i)). This thickness for the NRs layer is consistent with the previous work (3.37 μm) [16]. After the post-annealing treatment of the TiO_2 NRs–NFs layer, its thickness increased by ∼9% to 3.67 μm, while the total thickness of the fabricated photoanode film remained at ∼17 μm (Fig. 2(k)). The longer TiO_2 NRs are believed to have resulted from the second growth process during the annealing treatment; these NRs come from the Ti compound which still remains in the sample after hydrothermal growth [51]. This also in a good agreement with Selman et al. [59] and Muaz et al. [57], who reported obtaining longer film thicknesses after the annealing treatment. Based on the cross-section view, NFs were observed to be covered with NPs as shown by the orange circle (Fig. 2(k)). Further EDX analysis of mixed-phase TiO_2NRs–NFs/TiO_2 NPs shows higher Ti atomic percentage (29.03%) and lower O atomic percentage (70.97%) of ann film as compared to non-ann film (26.82 and 73.18%, respectively) as shown in Fig. 2(j) and 2(l). These differing atomic percentages are believed to be due to the annealing treatment, which not only contributed to the increase of film crystallinity but also to the diminishment of O content.

Meanwhile, the configuration morphology of a first hybrid photoanode film fabricated by spraying TC14-rGO on TiO_2 NRs–NFs/TiO_2 NPs (TiO_2 NRs–NFs/TiO_2 NPs/TC14-rGO) is shown in Fig. 2(m). In this image, the TC14-rGO particles are stacked on top of TiO_2 NPs and cover a significant portion of NPs as shown by the red circles surrounding the dark regions. The uncovered NPs are surrounded by green circles (brighter region) and indicate a drawback of using this process due to the smaller surface area available for dye adsorption. In order to counter this drawback, different configuration of photoanode film were synthesized by spraying TC14-rGO between the NRs–NFs and NPs (TiO_2 NRs–NFs/TC14-rGO/TiO_2 NPs). The top view of such a film is similar to the one shown in Fig. 2(h), while the cross-section is believed to be similar to the one shown in Fig. 2(k); the similarities are due to the thin layer of TC14-rGO, which is difficult to be observed.

The TC14-rGO layer serving as the hybrid material for the hybrid CE and photoanode is shown in Fig. 3(a). The thin basal plane of TC14-rGO is clearly discerned by the dark region in the image. Meanwhile, the transparent and folded up layer on the edge plane of the rGO layer as shown by the red arrow indicates the successful oxidation process promoted by the hyper-branched TC14 surfactant. The fold-up edge plane is also confirmed by the HRTEM image as shown in Fig. 3(b). Based on results from previous work [16], ∼2−4 layers were successfully produced by using this electrochemical exfoliation utilizing hyper-branched surfactant. This also been proven to give better performance as compared to the rGO produced by utilizing single-tail SDS surfactant [14–16]. The thin fold-up layer prevents the layers from restacking and increases the electrolyte diffusibility, thus improving the photovoltaic DSSCs performance [15,16,60]. When TC14-rGO was hybridized with MWCNTs and then coated by Pt NPs, the MWCNTs are prevented from agglomerating due to their strong adhesion to TC14-rGO (Fig. 3(c)). Simultaneously, MWCNTs also prevent the rGO layers from restacking [61]. The EDX analysis shown in Fig. 3(d) confirms the higher C atomic percentage (73.79%) of the hybrid film as compared to O atomic percentage (24.17%) is the marker of rGO, which is also consistent with previous work [51]. Moreover, the low Pt atomic percentage (2.04%) is due to the thin Pt coating (10 nm).

3.2. Micro-Raman spectroscopy

Fig. 4(a) presents micro-Raman spectra for both pure non- and ann TiO_2 NRs–NFs and also the mixed-phase TiO_2 NRs–NFs/TiO_2 NPs photoanode film. Based on the spectra shown in the bottom and middle part of Fig. 4(a), five peaks are clearly observed at 119 and 148 cm^{-1} (B_{1g}), 238 and 240 cm^{-1} (multiple phonon scattering), 446 and 447 cm^{-1} (E_g), 612 and 613 cm^{-1} (A_{1g}), and 694 and 696 cm^{-1} for non- and ann TiO_2 NRs–NFs, respectively. The rutile phase of the synthesized film was further confirmed by three relevant Raman active modes, which are expressed as $A_{1g}+ B_{1g}+ E_g$. A weak sharp peak at 119 and 148 cm^{-1} corresponding to the B_{1g} mode is caused by the symmetric bending vibration of O–Ti–O. Meanwhile, the anti-symmetric bending vibration results a sharp intense peak at 612 and 613 cm^{-1}. Another intense peak characteristic of the rutile phase arises at 446 and 447 cm^{-1}, which results from the O–Ti–O symmetric stretching vibration [62]. The nanometer scale of NRs–NFs was confirmed by the existence of a broad band peak at ∼238 and 240 cm^{-1} caused by multiple phonon scattering. Meanwhile, the small bump peak at ∼694 and 696 cm^{-1}further confirms the existence of the formed NFs shown by FESEM images (Fig. 2(c)) [63]. The red-shifted peak of ann TiO_2 NRs–NFs as compared to the non-ann sample is believed to be caused by the increment of compressive and tensile stress during the annealing treatment [36]. Next, after coating TiO_2 NPs on the TiO_2 NRs–NFs, four additional peaks representing the anatase phase are clearly observed in the range of 200–800 cm^{-1} [64,65]. The most intense peak at 144 cm^{-1} and the small peak at 198 cm^{-1} relates to the E_g mode. The two other peaks are 399 cm^{-1} (B_{1g}) and 518 cm^{-1} (A_{1g} ,B_{1g}), which confirms

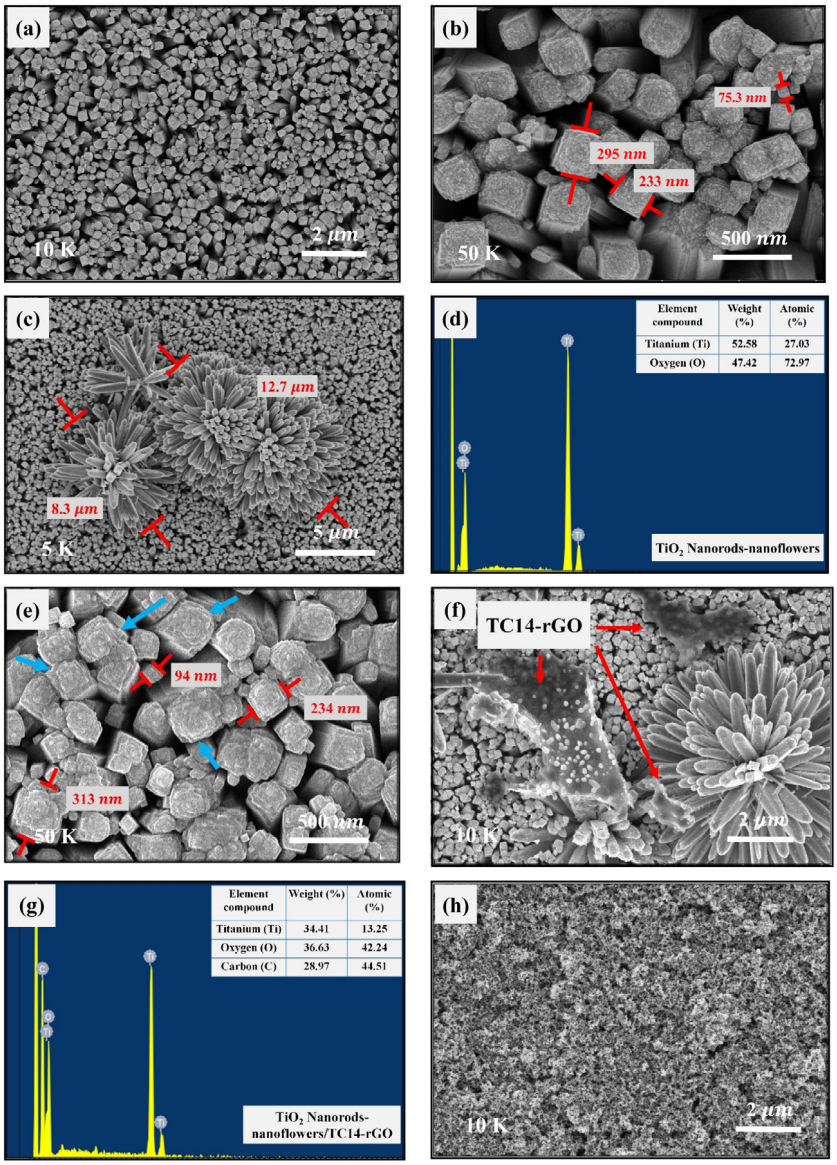

Fig. 2. FESEM images and EDX analysis of; (a)–(d) non-ann TiO_2 NRs–NFs, (e) ann TiO_2 NRs–NFs at 450 °C for 30 min, (f)–(g) TiO_2 NRs–NFs/TC14-rGO hybrid (h) TiO_2 NPs, cross section of (i)–(j) non-ann and (k)–(l) ann TiO_2 NRs–NFs/TiO_2 NPs, and (m) top view of TiO_2 NRs–NFs/TiO_2 NPs/TC14-rGO hybrid photoanode films.

the formation of crystalline TiO_2 [40]. Furthermore, when TC14-rGO was sprayed on the ann TiO_2 NRs–NFs sample, three peaks of Raman active modes were blue-shifted to lower wavelengths (144, 444, and 610 cm^{-1}) (Fig. 4(b)). In Fig. 4(b), the stacked rGO layer on TiO_2 NRs–NFs is indicated by two additional peaks at 1383 and 1589 cm^{-1}, which confirms the D- and G-bands of TC14-rGO. Their low peak intensities may be due to the small amount of TC14-rGO as compared to the TiO_2 NRs–NFs. The enlarged TC14-rGO peak presented in the inset of Fig. 4(b) implies a I_D/IG ratio of 0.68. A high I_D/IG ratio indicates a large number of defects confirmed by the wrinkled and fold-up layer morphology observed in the FESEM images (Fig. 3(a)).

The micro-Raman spectrum of the TC14-rGO_MWCNTs/Pt CE thin film is presented in Fig. 4(c). The low sharp peak observed at 242.3 cm^{-1} represents the A_{1g} symmetry radial breathing mode (RBM), which is characteristic of CNTs [66,67]. This also confirms a small intertube MWCNTs diameter of < 2 nm [52]. The intense laser irradiance used in the measurement generated a peak at 544.2 cm^{-1} [67]. The D-, G-, and 2D-band (characteristics of carbon material) are also clearly observed at 1344.8, 1573.2, and 2679.2 cm^{-1}, respectively; the calculated I_D/IG ratio is 0.41. The lower I_D/IG ratio of the hybrid film as compared to I_D/IG ratio of pristine TC14-rGO (0.70 of the previous result [16]) is due to the incorporation of the perfect sp^2 carbon structure of MWCNTs [66] and the Pt coating [51].

3.3. XRD analysis

The XRD patterns of fabricated TiO_2 NRs–NFs, TiO_2 NRs–NFs/TiO_2 NPs, and the hybridization with TC14-rGO by different configurations as the photoanode film are shown in Fig. 5. The bottom pattern (Fig. 5(a)) shows the rutile peaks of the pure non-ann TiO_2 NRs–NFs film; the intense peak arising at 27.83° represents the [110] plane. Three other discernible peaks are located at 36.49, 41.75, and 55.07°, which represent the [101], [111], and [211] planes of the rutile phase. After TiO_2 NPs were coated on non-ann TiO_2 NRs–NFs (Fig. 5(b)), an intense peak located at 25.65° [101] is seen, which is characteristic of the anatase phase. Two other discernible anatase peaks are

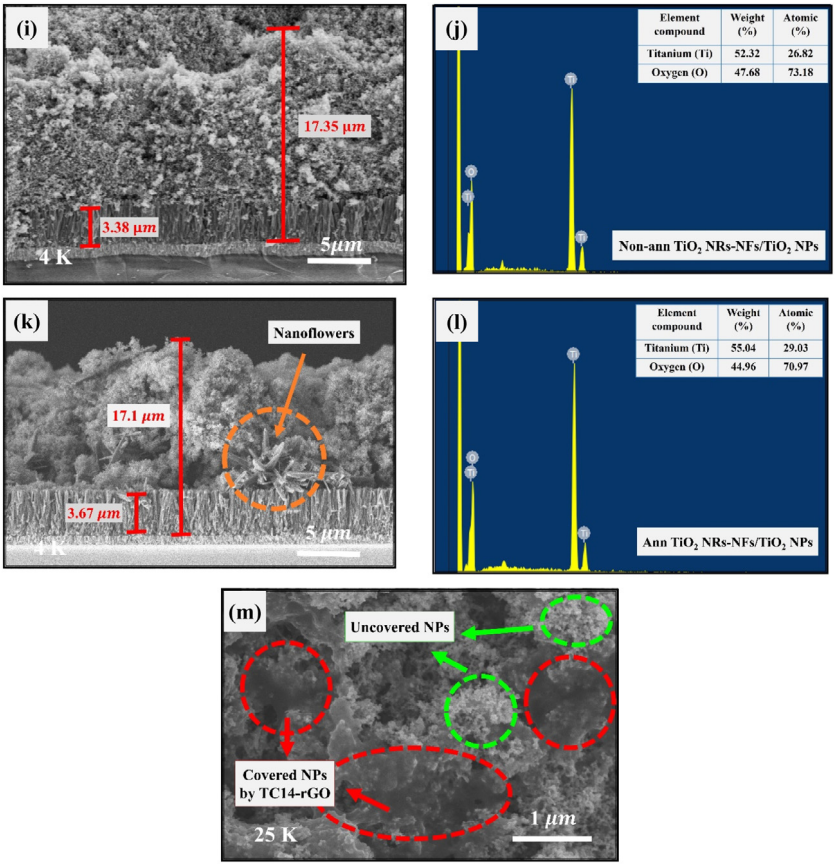

Fig. 2. (*continued*).

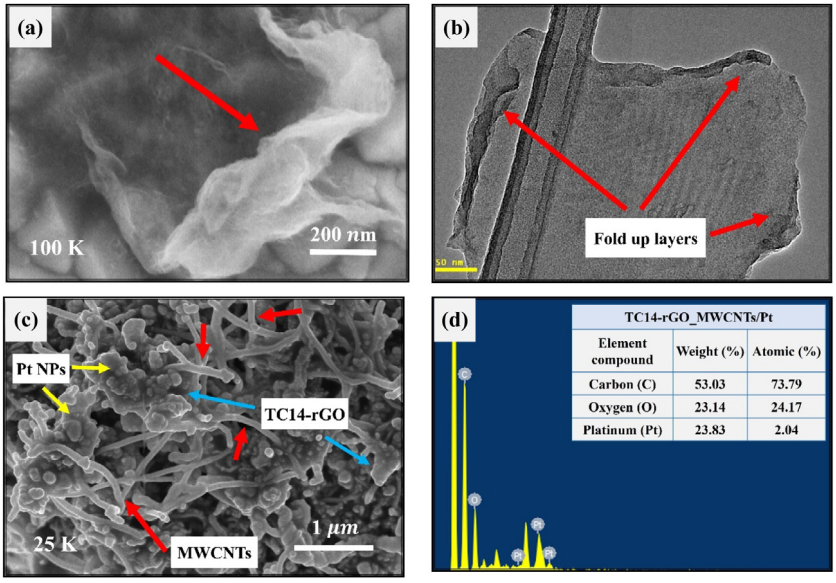

Fig. 3. (a)–(b) FESEM and HRTEM images of TC14-rGO and (c)–(d) top view and EDX analysis of TC14-rGO_MWCNTs/Pt as CE thin film.

observed at 38.97 and 48.38°, which represent the [004] and [200] planes, respectively. This further confirms the mixed-phase fabricated film as shown by micro-Raman spectra. The observed rutile and anatase peaks are in a good agreement with PDF No.01-071-4809 and PDF No.01-075-1537, respectively. All the rutile–anatase mixed-phase peaks remain and no obvious peak shifts can be detected in the ann TiO_2 NRs–NFs/TiO_2 NPs, TiO_2 NRs–NFs/TiO_2 NPs/TC14-rGO, and TiO_2 NRs–NFs/TC14-rGO/TiO_2 NPs samples shown in Fig. 5 (c)–(e). The C peak of TC14-rGO, which is normally detected at ∼25° was not detected in the hybrid photoanode films; this is believed to be due to its overlap with the anatase TiO_2 peak [39,68,69]. In addition, the thin layer resulting from the small amount of TC14-rGO and the thick

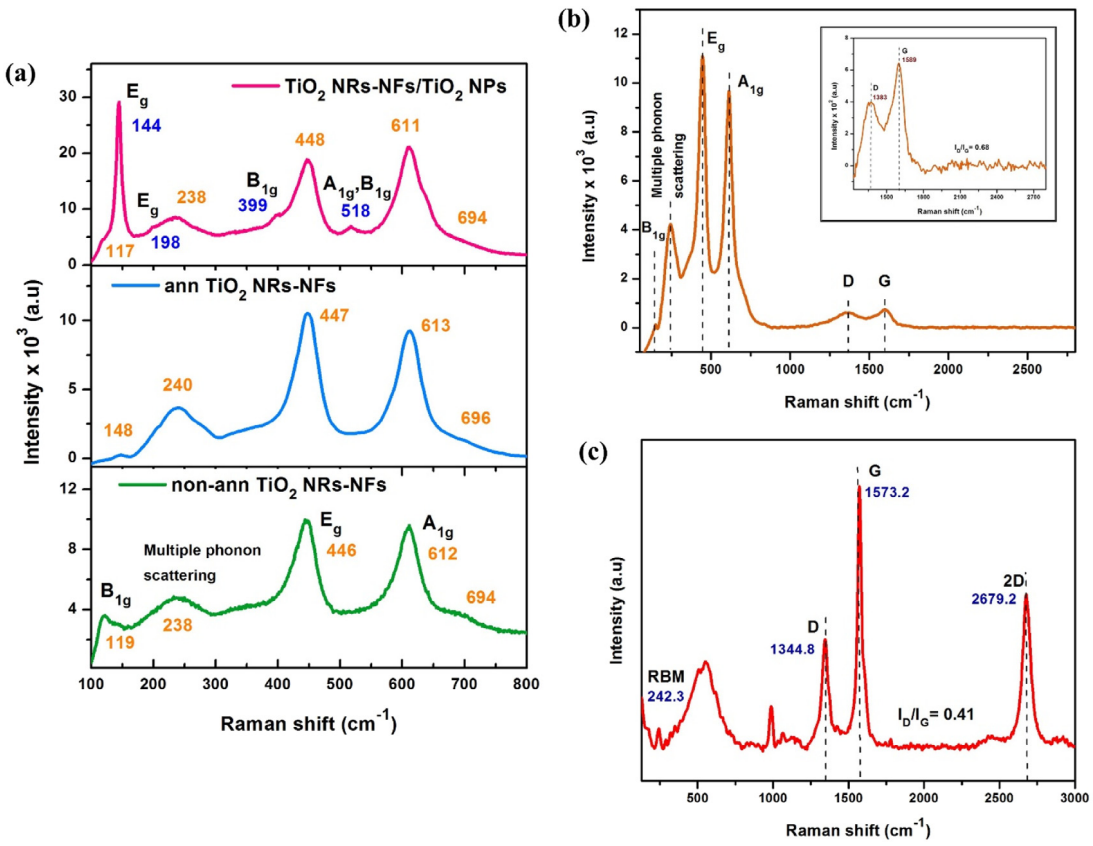

Fig. 4. Micro-Raman spectra of; (a) pure non- and ann TiO_2 NRs–NFs and mixed-phase TiO_2 NRs–NFs/TiO_2 NPs, (b) hybrid TiO_2 NRs–NFs/TC14-rGO with the insert picture showing the enlarged TC14-rGO peak, and (c) TC14-rGO_MWCNTs/Pt CE thin film.

layer of TiO_2 NPs as shown by FESEM images affect the laser penetration.

Additional crystallinity measurements reveal that pure non-ann TiO_2 NRs–NFs have a high crystallite percentage of 84%, which its four obvious peaks indicate the crystallinity to be over 85%. Moreover, the crystallite size implied by the obvious rutile peaks was found to be around 25−31 nm. The crystallite percentage of the films decreased to 78% when TiO_2 NPs were applied with the ratio between rutile and anatase phase was 26 and 74%, respectively. The lower crystallite percentage of the mixed-phase photoanode film can be easily attributed to the porous morphology of TiO_2 NPs as shown by FESEM images. Meanwhile, the crystallite size of pure anatase was 19−20 nm; its crystallite percentage indicated by the peaks was 85 and 87%, which is quite high for the fabricated film. The crystallite percentage of ann TiO_2 NRs–NFs/TiO_2 NPs slightly increased (79%) with the ratio between rutile and anatase phase was 21 and 79%. The bigger crystallite size of the rutile peak at 55−56° (40 nm) as compared to non-ann film (25 and 39 nm of pure and mixed-phase films, respectively) was caused by the annealing treatment [35,70]. The same crystallite percentage of 79% was also found for the hybrid TiO_2 NRs–NFs/TC14-rGO/TiO_2 NPs photoanode film.

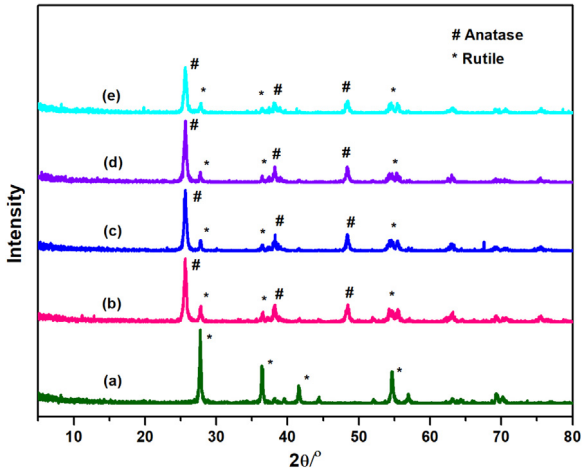

Fig. 5. XRD pattern of fabricated photoanode films; (a) non-ann TiO_2 NRs–NFs, (b) non-ann TiO_2 NRs–NFs/TiO_2 NPs, (c) ann TiO_2 NRs–NFs/TiO_2 NPs, (d) TiO_2 NRs–NFs/TiO_2 NPs/TC14-rGO, and (e) TiO_2 NRs–NFs/TC14-rGO/TiO_2 NPs.

3.4. I-V measurement

The resistivity comparison of pristine TC14-rGO, TC14-rGO_MWCNTs hybrid, and TC14-rGO_MWCNTs/Pt hybrid CE thin films is presented in Fig. 6. The high resistivity of pristine TC14-rGO (3.15 Ωcm) decreased when it was hybridized with WCPO-based MWCNTs (2.85 Ωcm). This was due to the incorporation of highly conductive MWCNTs by each TC14-rGO layer and thereby preventing the layers from restacking. This prevention decreased the internal resistance and provided faster electron pathways. In addition, based on previous work [16], TC14-rGO was also proven to give better conductivity as compared to the fabricated film utilizing single-tail SDS surfactant. The thin layer of TC14-rGO has fewer oxygen-containing functional groups as a result of the successful oxidation and reduction process for providing faster electron mobility. Lower resistivity (2.30 Ωcm) was further obtained after coating Pt NPs on the TC14-rGO_MWCNTs hybrid film. Small and uniform Pt NPs with less aggregation provide better electron transport due to their lower

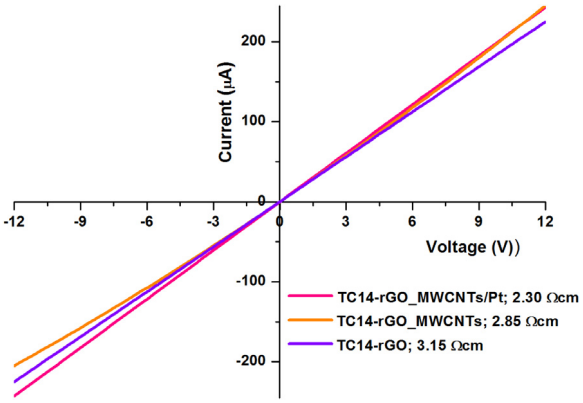

Fig. 6. The resistivity comparison of TC14-rGO, TC14-rGO_MWCNTs, and TC14-rGO_MWCNTs/Pt CE thin films by using four-point probes.

resistance [49]. The larger surface area of Pt NPs also resulted in better catalytic activity, which is beneficial for DSSCs application.

3.5. UV–Vis spectrophotometer

The transmittance of fabricated CE and photoanode films are presented in Fig. 7(a). Based on the spectra, the transmittance value of TC14-rGO_MWCNTs/Pt hybrid CE thin film was found to be 34.14%. Its relatively low transmittance value resulted from the low transmittance value of pristine Pt NPs and the dense bundled form of MWCNTs. Meanwhile, the transmittance value of the fabricated photoanode film was found to be < 3%. For the pure non-ann TiO_2 NRs–NFs film, a transmittance value of 1.51% caused from the dense and uniform synthesized film as shown by FESEM images. The transmittance further decreased to 0.87% after the synthesized film was annealed. This near-opacity may be caused by the structure refinement during the annealing treatment, which reduced the gap between the NRs and formed a uniformly arranged film. In addition, the surface roughness increased, which enhanced the light scattering effect and further decreased the transmittance [34,36]. When the ann pure TiO_2 NRs–NFs film was hybridized with TC14-rGO, its transmittance value increased to 1.53%. This may result from the existence of TC14-rGO, which is favorable for light harvesting [71]. The transmittance was further lowered when the TiO_2 NPs were applied on pure non-ann TiO_2 NRs–NFs (0.43%). Meanwhile, a similar low transmittance value of 0.39% was obtained for ann TiO_2 NRs–NFs/TiO_2 NPs, TiO_2 NRs–NFs/TC14-rGO/TiO_2 NPs and TiO_2 NRs–NFs/TiO_2 NPs/TC14-rGO hybrid films. This lower transmittance was due to the thick yet homogeneous TiO_2 NPs as presented in FESEM images.

Additional optical band gap energy (E_g) calculations based on Tauc's plot obtained from the intersection of the tangent line interpolation and the horizontal reference line [72] reveals the similar value of the theoretical rutile band gap (3.02 eV) of non-ann TiO_2 NRs–NFs [17]. This value decreased to 2.95 eV after the film was annealed as post-treatment after hydrothermal growth. The E_g value decrement suggests better electron transport and better electrical properties of the ann film (Fig. 7(b)), which is believed to be due to the increment of oxygen vacancies [56]. In addition, the annealing treatment improves the interconnection of NRs and NFs and thus improves the electron mobility [20]. This value then slightly decreased when the film was hybridized with TC14-rGO (2.93 eV). The thin TC14-rGO layer on the sample additionally enhances electron transport through the sample due to its good electrical properties. After TiO_2 NPs were applied on the synthesized pure and hybrid films, E_g decreased again. The non-ann TiO_2 NRs–NFs/TiO_2 NPs film exhibits a band gap value of 2.96 eV (from 3.02 eV for pure non-ann TiO_2 NRs–NFs), while the ann TiO_2 NRs–NFs/TiO_2 NPs film presents a lower band gap value of 2.92 eV (from 2.95 eV for pure ann TiO_2 NRs–NFs) (Fig. 7(c)). This once again confirms that the annealing treatment significantly affects the electrical properties of the fabricated film for the better performance. The band gap energy decrement of TiO_2 NRs–NFs/TiO_2 NPs was due to the synergistic effect of the mixed-phase TiO_2 film where the TiO_2 NRs–NFs and TiO_2 NPs were lying close to each other [73]. In addition, by applying the mixed-phase TiO_2 film, higher electron mobility and lower electron–hole recombination were achieved thus affect the band gap energy value [74]. As for the hybrid film (TiO_2 NRs–NFs/TiO_2 NPs/TC14-rGO), a higher E_g value of 2.94 eV indicates less efficiency for electron transport. The lowest E_g value of 2.89 eV for TiO_2 NRs–NFs/TC14-rGO/TiO_2 NPs suggests that this film has the fastest electron transport, rendering it effective for the application as the photoanode film. Concurrently, the TC14-rGO_MWCNTs/Pt CE film shows a low band gap value of 3.97 eV, which agrees well with the previous result [51]. Moreover, the high conductivity of small Pt NPs and MWCNTs adds to the overall conductivity of the CE film and thus decreases its E_g. The summaries of measured transmittance and E_g values of CE thin films are tabulated in Table 2.

Table 2
Transmittance and calculated E_g values of fabricated TC14-rGO_MWCNTs/Pt hybrid CE and various photoanode films.

Photoanode and CE thin films	Transmittance (%)	Band gap energy (E_g) (eV)
TC14-rGO_MWCNTs/Pt	34.14	3.97
Non-ann TiO_2 NRs–NFs	1.51	3.02
Ann TiO_2 NRs–NFs	0.87	2.95
Ann TiO_2 NRs–NFs/TC14-rGO	1.53	2.93
Non-ann TiO_2 NRs–NFs/TiO_2 NPs	0.43	2.96
Ann TiO_2 NRs–NFs/TiO_2 NPs	0.39	2.92
TiO_2 NRs–NFs/TC14-rGO/TiO_2 NPs	0.39	2.89
TiO_2 NRs–NFs/TiO_2 NPs/TC14-rGO	0.39	2.94

3.6. Solar simulator measurement

Four types of photoanode films used in this work are non-ann TiO_2 NRs–NFs/TiO_2 NPs, ann TiO_2 NRs–NFs/TiO_2 NPs, TiO_2 NRs–NFs/TiO_2 NPs/TC14-rGO, and TiO_2 NRs–NFs/TC14-rGO/TiO_2 NPs. The short circuit current density–voltage (J_{sc}-V) curves based on solar simulator measurements are presented in Fig. 8. Based on the measurement, non-ann TiO_2 NRs–NFs/TiO_2 NPs exhibits lower η, V_{oc}, and J_{sc} values of 1.215%, 0.738 V, and 3.078 mA/cm^2, respectively, as compared to the ann TiO_2 NRs–NFs/TiO_2 NPs film (1.462%, 0.756 V, and 3.765 mA/cm^2, respectively). Since the method to synthesize TiO_2 NPs was the same for all samples,

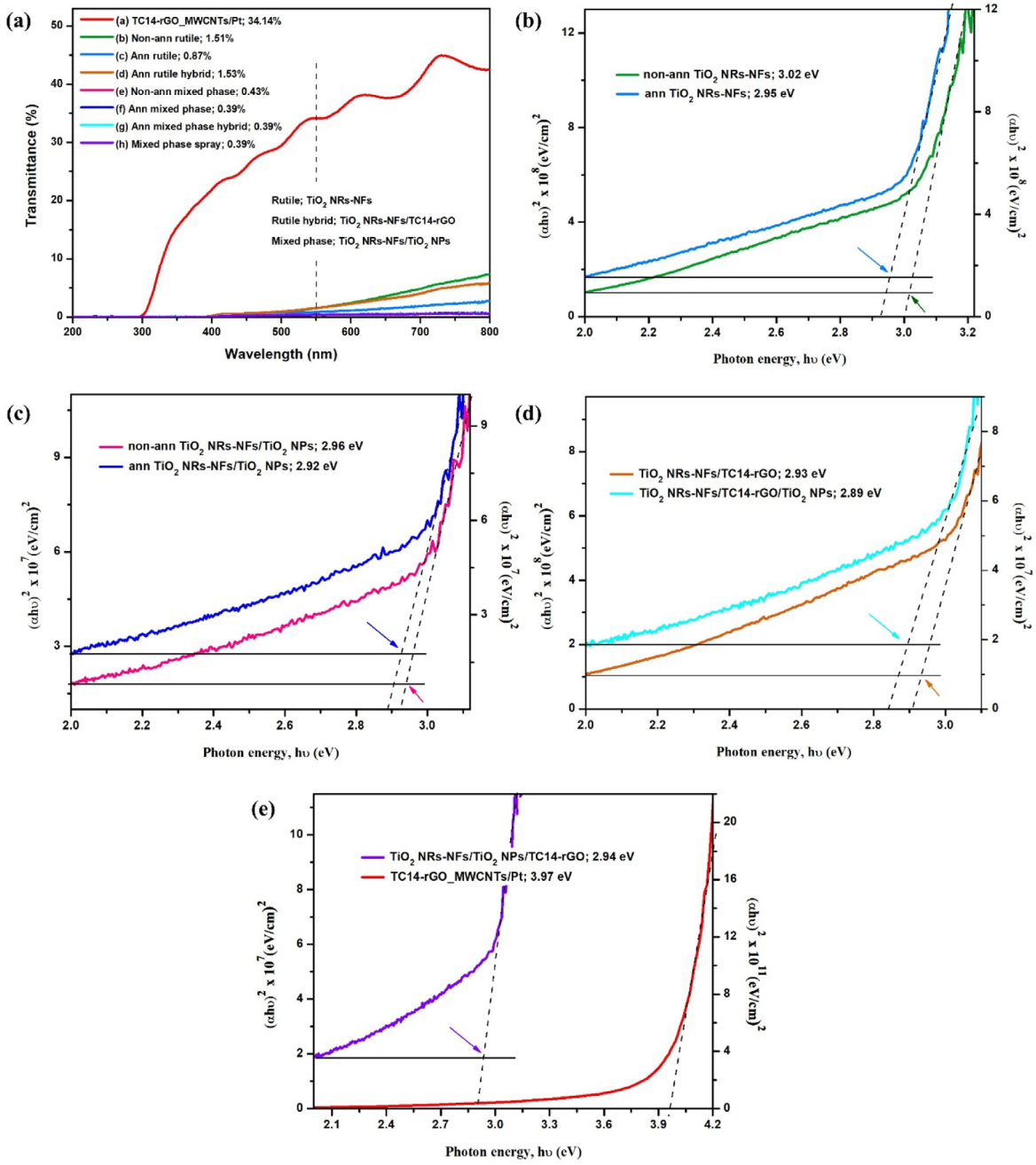

Fig. 7. (a) Transmittance measurements of CE and various photoanode films; calculated band gap energy of (b) non-ann and ann pure TiO_2 NRs-NFs, (c) ann TiO_2 NRs-NFs/TC14-rGO hybrid and non-ann TiO_2 NRs-NFs/TiO_2 NPs, (d) ann TiO_2 NRs-NFs/TiO_2 NPs and TiO_2 NRs-NFs/TC14-rGO/TiO_2 NPs, and (e) TiO_2 NRs–NFs/TiO_2 NPs/TC14-rGO hybrid photoanode film and TC14-rGO_MWCNTs/Pt CE hybrid thin film.

the possible reason for the different values between ann and non-ann samples could originate from the condition of the TiO_2 NRs–NFs. The post-annealing treatment of TiO_2 NRs–NFs as the photoanode bottom layer after hydrothermal growth increased the film crystallinity (confirmed by the higher crystallinity percentage and crystallite size for mixed-phase films), which further enhanced the V_{oc} and J_{sc} values [70]. In addition, potential surface contamination remaining after hydrothermal growth was further removed. The interconnection between NRs and NFs was strengthened by the annealing treatment [20], which may have decreased the electrical resistance and thus enhanced the electron mobility as proven by the lower E_g value of the annealed film. An NRs surface roughened by annealing enhanced the light scattering effect resulted in a higher electron injection and an increased J_{sc} value [36]. The greater J_{sc} value is also supported by the fact that the annealed film is shown to adsorb more dyes [20]. The higher V_{oc} value of the ann TiO_2 NRs–NFs/TiO_2 NPs film also suggests that the fabricated film has fewer defects and lower charge recombination [70].

When TC14-rGO was sprayed on the TiO_2 NRs–NFs/TiO_2 NPs film (TiO_2 NRs–NFs/TiO_2 NPs/TC14-rGO), DSSCs efficiency dropped to 0.525% and became the lowest η in comparison to other photoanode films. The much lower J_{sc} value (1.291 mA/cm^2) might be a result of less dye adsorption of TiO_2 NPs. The rGO coating had partially covered the TiO_2 NPs as shown by FESEM images [42,43]. The stacked TC14-rGO layer on TiO_2 NPs shortened penetration distance for the dye molecules and thus reduced the electron injection on TiO_2 NPs and TiO_2 NRs–NFs.

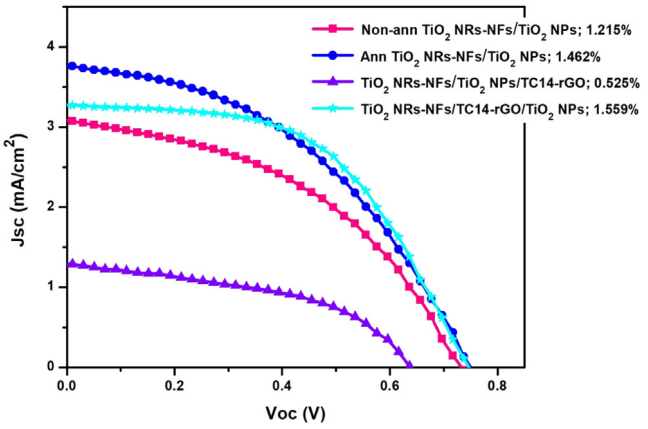

Fig. 8. Solar simulator measurement of DSSCs based on various kinds of photoanode films and on TC14-rGO_MWCNTs/Pt as the CE thin film.

Table 3
The photocurrent density–voltage characteristic curves of DSSCs fabricated with various types of photoanode films and with TC14-rGO_MWCNTs/Pt as the CE thin film.

Photoanode films	V_{oc} (V)	J_{sc} (mA/cm^2)	*FF* (%)	η (%)
Non-ann TiO_2 NRs–NFs/TiO_2 NPs	0.738	3.078	43.9	1.215
Ann TiO_2 NRs–NFs/TiO_2 NPs	0.756	3.765	43.2	1.462
TiO_2 NRs–NFs/TiO_2 NPs/TC14-rGO	0.647	1.291	47.2	0.525
TiO_2 NRs–NFs/TC14-rGO/TiO_2 NPs	0.747	3.275	53.5	1.559

This is supported by the higher E_g value of the TiO_2 NRs–NFs/TiO_2 NPs/TC14-rGO film, which indicates a slower electron transfer through the film. In contrast, when TC14-rGO was sprayed between TiO_2 NRs–NFs and TiO_2 NPs (TiO_2 NRs–NFs/TC14-rGO/TiO_2 NPs), η increased by ∼2× to 1.559%. This value also was calculated to be 28.3 and 6.6% higher as compared to non-ann and ann TiO_2 NRs–NFs/TiO_2 NPs, respectively, which suggests that TC14-rGO produced an incremental improvement in DSSCs performance. TC14-rGO has a role on facilitating the electron transfer from TiO_2 NPs to TiO_2 NRs–NFs and lessening the electron recombination. A thin layer of TC14-rGO in the middle photoanode layer enlarges film porosity and thus increases the electrolyte diffusibility [38]. The existence of TC14-rGO may also induce better electron transfer after photoexcitation occurs in the dyed semiconductor layer. This is believed to reduce the internal resistance and thus grant an advantage for faster electron transport through NPs before reaching the TiO_2 NRs–NFs layer and the TiO_2 NRs–NFs/TC14-rGO hybrid bottom layer. However, the drawback of applying rGO on TiO_2 also damages TiO_2 structure [40]. This is evidenced by lower J_{sc} (3.275 mA/cm^2) and V_{oc} values (0.747 V), as compared to ann TiO_2 NRs–NFs/TiO_2 NPs (see Table 3). The highest η value of TiO_2 NRs–NFs/TC14-rGO/TiO_2 NPs was supported by the highest fill factor (*FF*) value as compared to other photoanode films. The highest *FF* value indicates that the fabricated film has the lowest recombination rate with electrolytes, thus confirming the effectiveness of TC14-rGO [36].

The electron transmission in the hybrid TiO_2 NRs–NFs/TC14-rGO/TiO_2 NPs photoanode film can be explained from its conduction band (CB) as shown in Fig. 9(a). Based on the diagram, the excited electron from the dye is directly injected to the lower TiO_2 NPs conduction band (CB) and further transferred to the TC14-rGO layer due to its further lower CB than the TiO_2 NPs. Next, the slightly higher TiO_2 NRs CB (–4.41 eV) as compared to TC14-rGO CB (–4.43 eV) might restrain electron transmission. However, this is compensated by highly conductive TC14-rGO, which enables electrons to jump to the TiO_2 NRs and then rapidly transmit to the FTO substrate due to the vertically aligned TiO_2 NRs and lower CB of the FTO substrate. The restrained electrons on the boundary of TC14-rGO and TiO_2 NRs lower the electron transmission and become the reason for the diminished J_{sc} and V_{oc} values of DSSCs based on the TiO_2 NRs–NFs/TC14-rGO/TiO_2 NPs photoanode film. This is in stark contrast with the ann TiO_2 NRs–NFs/TiO_2 NPs sample. The lower CB from the top to the bottom photoanode layer (Fig. 9(b)) produced direct and fast electron transmission from the excited dye to the FTO substrate. This is proven by the highest J_{sc} and V_{oc} values of the sample. However, the large thickness of the TiO_2 NPs layer increased the electron recombination probability and thus lowered the *FF* value. Concurrently, the lowest η based on the TiO_2 NRs–NFs/TiO_2 NPs/TC14-rGO photoanode film was caused by the much higher CB of the TiO_2 NPs (–4.21 eV) as compared to the CB of TC14-rGO (–4.43 eV), which restrained the electron movement. Moreover, the low dye adsorption in TiO_2 NPs cannot be compensated by the small number of electrons from TC14-rGO, which resulted in the lowest J_{sc} value.

Overall, the high amount of dye adsorption is an outcome of the large thickness of the TiO_2 NPs as mentioned in the literatures [58,75,76]. This was supported by a fact that anatase TiO_2 NPs presents higher photocatalytic activity as compared to rutile TiO_2 NRs–NFs due to its strong adsorption ability on the surface which offers favorable site for the reaction [17]. These desired dimensions are produced by the optimal TTIP molarity used for TiO_2 NPs fabrication, which resulted in a porous morphology and a network of closely interconnected particles that are beneficial for dye adsorption and electron transfer, respectively. In addition, the wrinkled TC14-rGO structure led to enhanced electrolyte diffusibility for both photoanode and CE thin film [15,16]. The high conductivity of the hybrid TC14-rGO_MWCNTs/Pt CE film arises from the incorporation of highly conductive MWCNTs and Pt NPs. These two materials serve to increase electron mobility, which is crucial for improving DSSC performance. When MWCNTs bond to the TC14-rGO layer, they reduce the film resistance and help quicken electron transference. This also supported by the small size of Pt NPs, which is proven to yield better catalytic activity.

3.7. EIS analysis

The series resistance (R_s) and charge transfer resistance (R_{ct}) of fabricated DSSCs were measured by EIS analysis; results are presented in Fig. 10(a). In the inset figure, it is clearly seen that the lowest R_s value (80.24 Ω) was obtained from ann TiO_2 NRs–NFs/TiO_2 NPs. This indicates the lowest interfacial resistance and promotes effective carrier transport in the DSSCs device [77]. Moreover, this confirms that the post-annealing treatment of TiO_2 NRs–NFs significantly affects the electrical properties of the fabricated film. The highest R_s value (92.07 Ω) was achieved by TiO_2 NRs–NFs/TiO_2 NPs/TC14-rGO, which is attributed to the higher CB of TiO_2 NPs as compared to TC14-rGO as mentioned in the previous sub-section. More R_{ct} measurements show that TiO_2 NRs–NFs/TiO_2 NPs/TC14-rGO sample presents the highest R_{ct} value of 35 kΩ. The R_{ct} value is related to the charge transfer resistance, which indicates the lowest photovoltaic performance confirmed by the lowest η (0.525%) as compared to other samples. Conversely, the lowest R_{ct} value (13.93 kΩ) of TiO_2 NRs–NFs/TC14-rGO/TiO_2 NPs suggests the fastest electron transfer and lowest charge recombination, thus yielding the highest η (1.559%). This also confirmed by Bode plot shown in Fig. 10(b). Lower log frequency of TiO_2 NRs–NFs/TC14-rGO/TiO_2 NPs as compared to other samples indicates longer electron lifetime [78]. Moreover, the highest Bode plot of TiO_2 NRs–NFs/TiO_2 NPs/TC14-rGO suggests lower electron lifetime which resulted lowest η. A lower R_{ct} of ann TiO_2 NRs–NFs/TiO_2 NPs (27.25 kΩ) as compared to non-ann TiO_2 NRs–NFs/TiO_2 NPs (28.25 kΩ) confirms the higher η and better performance of the annealed film. The EIS analysis of fabricated DSSCs is summarized in Table 4.

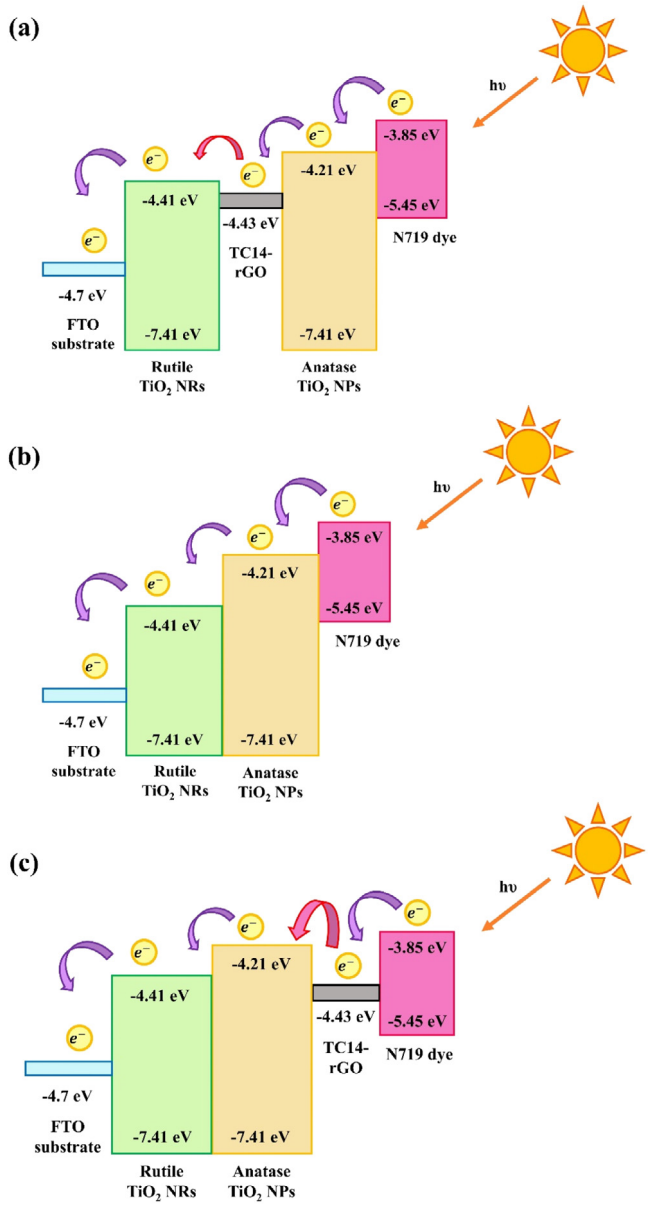

Fig. 9. Schematic diagram of electron transmission in photoanode based on (a) TiO_2 NRs–NFs/TC14-rGO/TiO_2 NPs, (b) TiO_2 NRs–NFs/TiO_2 NPs, and (c) TiO_2 NRs–NFs/TiO_2 NPs/TC14-rGO.

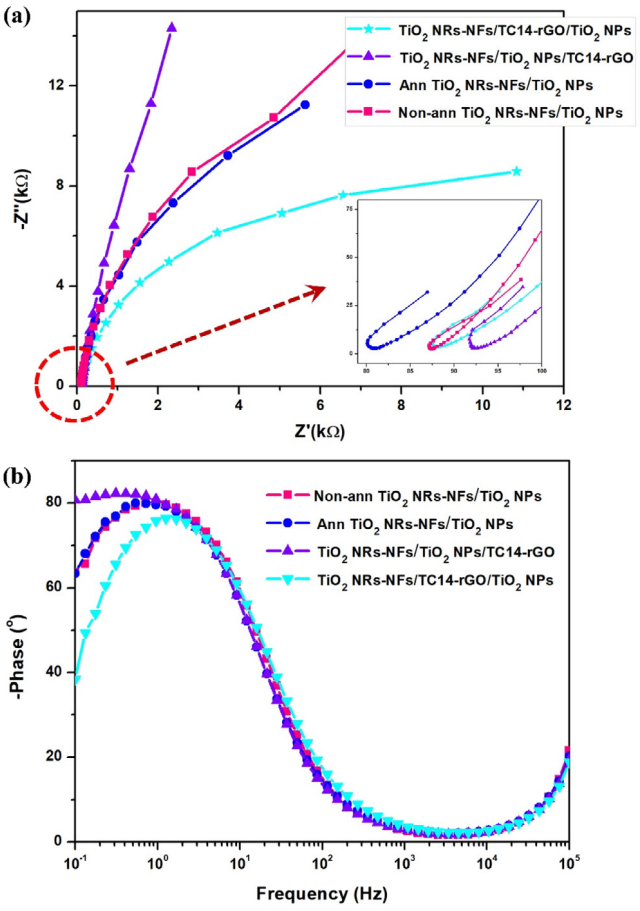

Fig. 10. (a) EIS analysis and (b) Bode plot of fabricated DSSCs.

Table 4
EIS analysis of DSSCs fabricated with various photoanode films and TC14-rGO_MWCNTs/Pt CE thin film.

Photoanode films	R_s (Ω)	R_{ct} (kΩ)
Non-ann TiO_2 NRs–NFs/TiO_2 NPs	87.22	28.25
Ann TiO_2 NRs–NFs/TiO_2 NPs	80.24	27.25
TiO_2 NRs–NFs/TiO_2 NPs/TC14-rGO	92.07	35.00
TiO_2 NRs–NFs/TC14-rGO/TiO_2 NPs	87.62	13.93

4. Conclusions

Various types of photoanode films were successfully fabricated using the simple and low-cost hydrothermal growth and squeegee method. Based on solar simulator measurements, the highest DSSCs efficiency was achieved by using TiO_2 NRs–NFs/TC14-rGO/TiO_2 NPs as photoanode (1.559%) with high V_{oc}, J_{sc}, and *FF* values of 0.747 V, 3.275 mA/cm2, and 53.5, respectively. This was due to the incorporation of TC14-rGO, which enhanced the electron transport and thus decreased the electron recombination. In addition, the thick TiO_2 NPs layer and the vertically aligned TiO_2 NRs layer provided a large surface area for dye adsorption and direct electron pathway, respectively. This also was supported by the utilization of a highly conductive TC14-rGO_MWCNTs/Pt hybrid CE film, which enhanced electron mobility. This result also shows that the annealing treatment after hydrothermal growth significantly enhanced DSSCs performance.

Acknowledgments

The authors would like to express their appreciation to the TWAS-COMSTECH Joint Research, Italy Grant (Grant code: 2017-0001-102-11) and Fundamental Research Grant Scheme, Malaysia (Grant code: 2015-0154-102-02) for the financial support.

Declaration of interests

The authors declare that they have no known competing financial interests or personal relationships that could have appeared to influence the work reported in this paper.

References

[1] M.A. Green, K. Emery, Y. Hishikawa, W. Warta, E.D. Dunlop, Solar cell efficiency tables (version 44), Prog. Photovolt. Res. Appl. 22 (2014) 701–710, http://dx.doi.org/10.1002/pip.

[2] M. Bokalič, M. Topič, Spatially Resolved Characterization in Thin-Film Photovoltaics, Springer US, New York, 2015, http://dx.doi.org/10.1007/978-3-319-14651-5.

[3] B. O'Regan, M. Grätzel, A low-cost, high-efficiency solar-cell based on dye-sensitized colloidal TiO_2 films, Nature 353 (1991) 737–740, http://dx.doi.org/10.1038/353737a0.

[4] M. Zhu, X. Li, W. Liu, Y. Cui, An investigation on the photoelectrochemical properties of dye-sensitized solar cells based on graphene- TiO_2 composite photoanodes, J. Power Sources 262 (2014) 349–355, http://dx.doi.org/10.1016/j.jpowsour.2014.04.001.

[5] D. Qin, Y. Bi, X. Feng, W. Wang, G.D. Barber, T. Wang, Y. Song, X. Lu, T.E. Mallouk, Hydrothermal growth and photoelectrochemistry of highly oriented, crystalline anatase TiO_2 nanorods on transparent conducting electrodes, Chem. Mater 27 (2015) 4180–4183, http://dx.doi.org/10.1021/acs.chemmater.5b00782.

[6] E. Demir, B. Sen, F. Sen, Highly efficient pt nanoparticles and f-MWCNT nanocomposites based counter electrodes for dye-sensitized solar cells, Nano-Struct. Nano-Objects. 11 (2017) 39–45, http://dx.doi.org/10.1016/j.nanoso.2017.06.003.

[7] K. Kakiage, Y. Aoyama, T. Yano, K. Oya, J. Fujisawa, M. Hanaya, Highly-efficient dye-sensitized solar cells with collaborative sensitization by silyl-anchor and carboxy-anchor dyes, Chem. Commun. 51 (2015) 15894–15897, http://dx.doi.org/10.1039/C5CC06759F.

[8] D. Wang, X. Zhu, Y. Fang, J. Sun, C. Zhang, X. Zhang, Simultaneously composition and interface control for ZnO-based dye-sensitized solar cells with highly enhanced efficiency, Nano-Struct. Nano-Objects 10 (2017) 1–8, http://dx.doi.org/10.1016/j.nanoso.2017.01.001.

[9] S.G. Ullattil, A.V. Thelappurath, S.N. Tadka, J. Kavil, B.K. Vijayan, P. Periyat, A sol-solvothermal processed 'Black TiO_2' as photoanode material in dye sensitized solar cells, Sol. Energy 155 (2017) 490–495, http://dx.doi.org/10.1016/j.solener.2017.06.059.

[10] S.G. Ullattil, P. Periyat, Microwave-power induced green synthesis of randomly oriented mesoporous anatase TiO_2 nanoparticles for efficient dye sensitized solar cells, Sol. Energy 147 (2017) 99–105, http://dx.doi.org/10.1016/j.solener.2017.03.039.

[11] J.-F. Wang, J.-J. Zhang, D.-N. He, Flower-like TiO_2-B particles wrapped by graphene with different contents as an anode material for lithium-ion batteries, Nano-Struct. Nano-Objects 15 (2018) 216–223, http://dx.doi.org/10.1016/j.nanoso.2018.03.008.

[12] M. Quintana, T. Edvinsson, A. Hagfeldt, G. Boschloo, Comparison of dye-sensitized ZnO and TiO_2 solar cells : studies of charge transport and carrier lifetime, J. Phys. Chem. C. 111 (2007) 1035–1041.

[13] Y. Xie, X. Zhou, H. Mi, J. Ma, J. Yang, J. Cheng, High efficiency ZnO-based dye-sensitized solar cells with a 1H, 1H, 2H, 2H-perfluorodecyltriethoxysilane chain barrier for cutting on interfacial recombination, Appl. Surf. Sci. 434 (2018) 1144–1152, http://dx.doi.org/10.1016/j.apsusc.2017.11.075.

[14] A.B. Suriani, . Fatiatun, A. Mohamed, . Muqoyyanah, N. Hashim, M.S. Rosmi, M.H. Mamat, M.F. Malek, M.J. Salifairus, H.P.S. Abdul Khalil, Reduced graphene oxide/platinum hybrid counter electrode assisted by custom-made triple-tail surfactant and zinc oxide/titanium dioxide bilayer nanocomposite photoanode for enhancement of DSSCs photovoltaic performance, Opt. J. Light Electron Opt. 161 (2018) 70–83, http://dx.doi.org/10.1016/j.ijleo.2018.02.013.

[15] A.B. Suriani, M.D. Nurhafizah, A. Mohamed, M.H. Mamat, M.F. Malek, M.K. Ahmad, A. Pandikumar, N.M. Huang, Enhanced photovoltaic performance using reduced graphene oxide assisted by triple-tail surfactant as an efficient and low-cost counter electrode for dye-sensitized solar cells, Opt. - Int. J. Light Electron Opt. 139 (2017) 291–298, http://dx.doi.org/10.1016/j.ijleo.2017.04.025.

[16] A.B. Suriani, . Muqoyyanah, A. Mohamed, M.H. Mamat, N. Hashim, I.M. Isa, M.F. Malek, M.I. Kairi, A.R. Mohamed, M.K. Ahmad, Improving the photovoltaic performance of DSSCs using a combination of mixed-phase TiO_2 nanostructure photoanode and agglomerated free reduced graphene oxide counter electrode assisted with hyperbranched surfactant, Opt. - Int. J. Light Electron Opt. 158 (2018) 522–534, http://dx.doi.org/10.1016/j.ijleo.2017.12.149.

[17] J. Lei, H. Li, J. Zhang, M. Anpo, Mixed-phase TiO_2 nanomaterials as efficient photocatalysts, in: Low Dimensional and Nanostructured Materials and Devices, Springer, Switzerland, 2016, http://dx.doi.org/10.1007/978-3-319-25340-4.

[18] J.-Y. Liao, J.-W. He, H. Xu, D.-B. Kuang, C.-Y. Su, Effect of TiO_2 morphology on photovoltaic performance of dye-sensitized solar cells: nanoparticles, nanofibers, hierarchical spheres and ellipsoid spheres, J. Mater. Chem. 22 (2012) 7910–7918, http://dx.doi.org/10.1039/c2jm16148f.

[19] D. Zhang, T. Yoshida, T. Oekermann, K. Furuta, H. Minoura, Room-temperature synthesis of porous nanoparticulate TiO_2 films for flexible dye-sensitized solar cells, Adv. Funct. Mater. 16 (2006) 1228–1234, http://dx.doi.org/10.1002/adfm.200500700.

[20] M.K. Ahmad, C.F. Soon, N. Nafarizal, A.B. Suriani, A. Mohamed, M.H. Mamat, M.F. Malek, M. Shimomura, K. Murakami, Effect of heat treatment to the rutile based dye sensitized solar cell, Opt. - Int. J. Light Electron Opt. J. Light Electron Opt. 127 (2016) 4076–4079, http://dx.doi.org/10.1016/j.ijleo.2016.01.034.

[21] A.Q.D. Faisal, Synthesis and characteristics study of TiO_2 nanowires and nanoflowers on FTO/glass and glass substrates via hydrothermal technique, J. Mater. Sci. Mater. Electron. 26 (2015) 317–321, http://dx.doi.org/10.1007/s10854-014-2402-4.

[22] J. Hu, J. Cheng, S. Tong, L. Zhao, J. Duan, Y. Yang, Dye-sensitized solar cells based on P25 nanoparticles/ TiO_2 nanotube arrays/hollow TiO_2 boxes three-layer composite film, J. Mater. Sci. Mater. Electron. 27 (2016) 5362–5370, http://dx.doi.org/10.1007/s10854-016-4436-2.

[23] M.K. Ahmad, K. Murakami, Rutile-phased TiO_2 nanorods/nanoflowers based dye-sensitized solar cell, Appl. Mech. Mater. 773–774 (2015) 725–728, http://dx.doi.org/10.4028/www.scientific.net/AMM.

[24] S.-C. Yang, D.-J. Yang, J. Kim, J.-M. Hong, H.-G. Kim, I.-D. Kim, H. Lee, Hollow TiO_2 hemispheres obtained by colloidal templating for application in dye-sensitized solar cells, Adv. Mater. 20 (2008) 1059–1064, http://dx.doi.org/10.1002/adma.200701808.

[25] J. Wang, S. Qu, Z. Zhong, S. Wang, K. Liu, A. Hu, Fabrication of TiO_2 nanoparticles/nanorod composite arrays via a two-step method for efficient dye-sensitized solar cells, Prog. Nat. Sci. Mater. Int. 24 (2014) 588–592, http://dx.doi.org/10.1016/j.pnsc.2014.10.013.

[26] Y. Cao, Z. Li, Y. Wang, T. Zhang, Y. Li, X. Liu, F. Li, Influence of TiO_2 nanorod arrays on the bilayered photoanode for dye-sensitized solar cells, J. Electron. Mater. 45 (2016) 4989–4998, http://dx.doi.org/10.1007/s11664-016-4670-7.

[27] S. Sadhu, P. Poddar, Template-free fabrication of highly-oriented single-crystalline 1D-rutile TiO_2-MWCNT composite for enhanced photoelectrochemical activity, J. Phys. Chem. C. 118 (2014) 19363–19373, http://dx.doi.org/10.1021/jp5023983.

[28] W. Wu, J. Liao, H. Chen, X. Yu, C. Su, D. Kuang, Dye-sensitized solar cells based on a double layered TiO_2 photoanode consisting of hierarchical nanowire arrays and nanoparticles with greatly improved photovoltaic performance, J. Mater. Chem. 22 (2012) 18057–18062, http://dx.doi.org/10.1039/c2jm33829g.

[29] J. Su, L. Guo, High aspect ratio TiO_2 nanowires tailored in concentrated HCl hydrothermal condition for photoelectrochemical water splitting, RSC Adv. 5 (2015) 53012–53018, http://dx.doi.org/10.1039/b000000x.

[30] H. Hafez, Z. Lan, Q. Li, J. Wu, High efficiency dye-sensitized solar cell based on novel TiO_2 nanorod/nanoparticle bilayer electrode, Nanotechnol. Sci. Appl. 3 (2010) 45–51, http://dx.doi.org/10.2147/NSA.S11350.

[31] M.K. Ahmad, M. Kenji, Effect of anatase TiO_2 overlayer on the photovoltaic properties of rutile phase nanostructured dye-sensitized solar cell, Micro Nanoelectron. 2 (2013) 262–264.

[32] F. Rezvani, E. Parvazian, S.A. Hosseini, Dye-sensitized solar cells based on composite TiO_2 nanoparticle–nanorod single and bi-layer photoelectrodes, Bull. Mater. Sci. 39 (2016) 1397–1402, http://dx.doi.org/10.1007/s12034-016-1278-8.

[33] K. Ahn, H. Lee, Y. Jeong, J. Kim, S. Jeong, C. Cho, Effects of TiO_2 nanorod length and post-annealing on the electrical properties of TiO_2 nanobarbed fiber structures, J. Nanosci. Nanotechnol. 11 (2011) 7155–7158, http://dx.doi.org/10.1166/jnn.2011.4847.

[34] M.M. Hasan, A.S.M.A. Haseeb, R. Saidur, H.H. Masjuki, Effects of annealing treatment on optical properties of anatase TiO_2 thin films, Int. J. Mech. Aerospace, Ind. Mechatron. Manuf. Eng. 2 (2008) 410–414.

[35] D. Zhao, T. Peng, L. Lu, P. Cai, P. Jiang, Z. Bian, Effect of annealing temperature on the photoelectrochemical properties of dye-sensitized solar cells made with mesoporous TiO_2 nanoparticles, J. Phys. Chem. C. 112 (2008) 8486–8494.

[36] L. Meng, C. Li, M.P. dos Santos, Effect of annealing temperature on TiO_2 nanorod films prepared by dc reactive magnetron sputtering for dye-sensitized solar cells, J. Inorg. Organomet. Polym. Mater. 21 (2011) 770–776, http://dx.doi.org/10.1007/s10904-011-9538-y.

[37] U. Mehmood, Z. Malaibari, F.A. Rabani, A.U. Rehman, S.H.A. Ahmad, M.A. Atieh, M.S. Kamal, Photovoltaic improvement and charge recombination reduction by aluminum oxide impregnated MWCNTs/ TiO_2 based photoanode for dye-sensitized solar cells, Electrochim. Acta. 203 (2016) 162–170, http://dx.doi.org/10.1016/j.electacta.2016.04.027.

[38] A.M. Ilyas, M.A. Gondal, U. Baig, S. Akhtar, Z.H. Yamani, Photovoltaic performance and photocatalytic activity of facile synthesized graphene decorated TiO_2 monohybrid using nanosecond pulsed ablation in liquid technique, Sol. Energy 137 (2016) 246–255, http://dx.doi.org/10.1016/j.solener.2016.08.019.

[39] S.-B. Kim, J.-Y. Park, C.-S. Kim, K. Okuyama, S.-E. Lee, H.-D. Jang, T.-O. Kim, Effects of graphene in dye-sensitized solar cells based on nitrogen-doped TiO_2 composite, J. Phys. Chem. C. 119 (2015) 16552–16559, http://dx.doi.org/10.1021/acs.jpcc.5b02309.

[40] L. Liu, Y. Zhang, B. Zhang, Y. Feng, A detailed investigation on the performance of dye-sensitized solar cells based on reduced graphene oxide-doped TiO_2 photoanode, J. Mater. Sci. 52 (2017) 8070–8083, http://dx.doi.org/10.1007/s10853-017-1014-9.

[41] J. Song, Z. Yin, Z. Yang, P. Amaladass, S. Wu, J. Ye, Y. Zhao, W.-Q. Deng, H. Zhang, X.-W. Liu, Enhancement of photogenerated electron transport in dye-sensitized solar cells with introduction of a reduced graphene oxide- TiO_2 junction, Chem. - A Eur. J. 17 (2011) 10832–10837, http://dx.doi.org/10.1002/chem.201101263.

[42] J. Liu, X. Fu, D.-P. Cao, L. Mao, J. Wang, D. Mu, B. Mi, B. Zhao, Z. Gao, Stacked graphene– TiO_2 photoanode via electrospray deposition for highly efficient dye-sensitized solar cells, Org. Electron. 23 (2015) 158–163, http://dx.doi.org/10.1016/j.orgel.2015.04.021.

[43] J. Zhao, J. Wu, M. Zheng, J. Huo, Y. Tu, Improving the photovoltaic performance of dye-sensitized solar cell by graphene/titania photoanode, Electrochim. Acta. 156 (2015) 261–266, http://dx.doi.org/10.1016/j.electacta.2015.01.045.

[44] S. Yuan, S. Chen, Z. Hu, G. Jiang, Y. Zhang, Y. Yang, P. Xiong, X. Zhu, J. Xiong, Reduced graphene oxide and carbon/elongated TiO_2 nanotubes composites as anodes for Li-ion batteries, Nano-Struct. Nano-Objects. 12 (2017) 27–32, http://dx.doi.org/10.1016/j.nanoso.2017.08.015.

[45] A. Morais, S. do A. Carminati, A.F. Nogueira, Nanostructured hybrid materials based on reduced graphene oxide for solar energy conversion, Int. Soc. Opt. Photonics (2016) 1–14, http://dx.doi.org/10.1117/12.2240029.

[46] P. Wang, F. He, J. Wang, H. Yu, L. Zhao, Graphene oxide nanosheets as an effective template for the synthesis of porous TiO_2 film in dye-sensitized solar cells, Appl. Surf. Sci. 358 (Part) (2015) 175–180, http://dx.doi.org/10.1016/j.apsusc.2015.06.102.

[47] S.A. Kazmi, S. Hameed, A.S. Ahmed, M. Arshad, A. Azam, Electrical and optical properties of graphene – TiO_2 nanocomposite and its applications in dye sensitized solar cells (DSSC), J. Alloys Compd. (2016) http://dx.doi.org/10.1016/j.jallcom.2016.08.319.

[48] E. Demir, A. Savk, B. Sen, F. Sen, A novel monodisperse metal nanoparticles anchored graphene oxide as counter electrode for dye-sensitized solar cells, Nano-Struct. Nano-Objects. 12 (2017) 41–45, http://dx.doi.org/10.1016/j.nanoso.2017.08.018.

[49] M.Y. Song, K.N. Chaudhari, J. Park, D. Yang, J.H. Kim, M. Kim, K. Lim, J. Ko, J. Yu, High efficient pt counter electrode prepared by homogeneous deposition method for dye-sensitized solar cell, Appl. Energy. 100 (2012) 132–137, http://dx.doi.org/10.1016/j.apenergy.2012.06.017.

[50] M.-H. Yeh, L.-Y. Lin, C.-L. Sun, Y.-A. Leu, J.-T. Tsai, C.-Y. Yeh, R. Vittal, K.-C. Ho, Multiwalled carbon nanotube@reduced graphene oxide nanoribbon as the counter electrode for dye-sensitized solar cells, J. Phys. Chem. C. 118 (2014) 16626–16634.

[51] A.B. Suriani, . Muqoyyanah, A. Mohamed, M.H.D. Othman, M.H. Mamat, N. Hashim, M.K. Ahmad, N. Nayan, H.P.S.A. Khalil, Reduced graphene oxide-multiwalled carbon nanotubes hybrid film with low pt loading as counter electrode for improved photovoltaic performance of dye-sensitised solar cells, J. Mater. Sci. Mater. Electron. 29 (2018) 10723–10743, http://dx.doi.org/10.1007/s10854-018-9139-4.

[52] A.B. Suriani, J. Norhafizah, A. Mohamed, M.H. Mamat, M.F. Malek, M.K. Ahmad, Scaled-up prototype of carbon nanotube production system utilizing waste cooking palm oil precursor and its nanocomposite application as supercapacitor electrodes, J. Mater. Sci. Mater. Electron. 27 (2016) 11599–11605, http://dx.doi.org/10.1007/s10854-016-5291-x.

[53] M.S. Azmina, A.B. Suriani, A.N. Falina, M. Salina, M. Rusop, Temperature effects on the production of carbon nanotubes from palm oil by thermal chemical vapor deposition method, Nanomater. Synth. Charact. 364 (2012) 359–362, http://dx.doi.org/10.4028/www.scientific.net/AMR.364.359.

[54] W. Zhou, X. Liu, J. Cui, D. Liu, J. Li, H. Jiang, J. Wang, H. Liu, Control synthesis of rutile TiO_2 microspheres, nanoflowers, nanotrees and nanobelts via acid-hydrothermal method and their optical properties, CrystEngComm. 13 (2011) 4557–4563, http://dx.doi.org/10.1039/c1ce05186e.

[55] A. Kumar, A.R. Madaria, C. Zhou, Growth of aligned single-crystalline rutile TiO_2 nanowires on arbitrary substrates and their application in dye-sensitized solar cells, J. Phys. Chem. C. 114 (2010) 7787–7792, http://dx.doi.org/10.1021/jp100491h.

[56] B. Wang, H. Qi, H. Wang, Y. Cui, J. Zhao, J. Guo, Y. Cui, Y. Liu, K. Yi, J. Shao, Morphology, Structure and optical properties in TiO_2 nanostructured films annealed at various temperatures, Opt. Mater. Express. 5 (2015) 1410–1418, http://dx.doi.org/10.1364/OME.5.001410.

[57] A.K.M. Muaz, U. Hashim, F. Ibrahim, K.L. Thong, M.S. Mokhtar, W.-W. Liu, Effect of annealing temperatures on the morphology, optical and electrical properties of TiO_2 thin films synthesized by the sol–gel method and deposited on Al/TiO_2/SiO_2/p-Si, Microsyst. Technol. (2015) http://dx.doi.org/10.1007/s00542-015-2514-7.

[58] J.K. Tsai, W.D. Hsu, T.C. Wu, T.H. Meen, W.J. Chong, Effect of compressed TiO_2 nanoparticle thin film thickness on the performance of dye-sensitized solar cells, Nanoscale Res. Lett. 8 (2013) 1–6.

[59] A.M. Selman, Z. Hassan, Effect of annealing treatment on growth of rutile TiO_2 nanorods prepared by chemical bath deposition method on silicon substrate, Appl. Mech. Mater. 624 (2014) 129–133, http://dx.doi.org/10.4028/www.scientific.net/AMM.624.129.

[60] Q. Zhang, Y. Liu, Y. Duan, N. Fu, Q. Liu, Y. Fang, Q. Sun, Y. Lin, Mn_3O_4/graphene composite as counter electrode in dye-sensitized solar cells, RSC Adv. 4 (2014) 15091–15097, http://dx.doi.org/10.1039/c4ra00347k.

[61] S.H. Aboutalebi, A.T. Chidembo, M. Salari, K. Konstantinov, D. Wexler, H.K. Liu, S.X. Dou, Comparison of GO, GO/MWCNTs composite and MWCNTs as potential electrode materials for supercapacitors, Energy Environ. Sci. 4 (2011) 1855–1865, http://dx.doi.org/10.1039/c1ee01039e.

[62] J. Yan, G. Wu, N. Guan, L. Li, Z. Li, X. Cao, Understanding the effect of surface/bulk defects on the photocatalytic activity of TiO_2: anatase versus rutile, Phys. Chem. Chem. Phys. 15 (2013) 10978, http://dx.doi.org/10.1039/c3cp50927c.

[63] M.K. Ahmad, S.M. Mokhtar, C.F. Soon, N. Nafarizal, A.B. Suriani, A. Mohamed, M.H. Mamat, M.F. Malek, M. Shimomura, K. Murakami, Raman investigation of rutile-phased TiO_2 nanorods/nanoflowers with various reaction times using one step hydrothermal method, J. Mater. Sci. Mater. Electron. 27 (2016) 7920–7926, http://dx.doi.org/10.1007/s10854-016-4783-z.

[64] U. Balachandran, N.G. Eror, Raman spectra of titanium dioxide, J. Solid State Chem. 42 (1982) 276–282.

[65] R.J. Meier, Vibrational spectroscopy : a 'vanishing' discipline?, Chem. Soc. Rev. 34 (2005) 743–752, http://dx.doi.org/10.1039/b503880d.

[66] J.-J. Shao, W. Lv, Q. Guo, C. Zhang, Q. Xu, Q.-H. Yang, F. Kang, Hybridization of graphene oxide and carbon nanotubes at the liquid/air interface, Chem. Commun. 48 (2012) 3706–3709, http://dx.doi.org/10.1039/c1cc16838j.

[67] J.H. Lehman, M. Terrones, E. Mansfield, K.E. Hurst, V. Meunier, Evaluating the characteristics of multiwall carbon nanotubes, Carbon N. Y. 49 (2011) 2581–2602, http://dx.doi.org/10.1016/j.carbon.2011.03.028.

[68] T. Lan, H. Qiu, F. Xie, J. Yang, M. Wei, Rutile TiO_2 mesocrystals/reduced graphene oxide with high-rate and long-term performance for lithium-ion batteries, Mater. Energy Catal. 5 (2015) 1–6, http://dx.doi.org/10.1038/srep08498.

[69] P. Zhu, A.S. Nair, P. Shengjie, Y. Shengyuan, S. Ramakrishna, Facile fabrication of TiO_2—graphene composite with enhanced photovoltaic and photocatalytic properties by electrospinning, ACS Appl. Mater. Interfaces 4 (2012) 581–585, http://dx.doi.org/10.1021/am201448p.

[70] R. Keshavarzi, V. Mirkhani, M. Moghadam, S. Tangestaninejad, I. Mohammadpoor-Baltork, Performance enhancement of dye-sensitized solar cells based on TiO_2 thick mesoporous photoanodes by morphological manipulation, Langmuir. 31 (2015) 11659–11670, http://dx.doi.org/10.1021/acs.langmuir.5b02718.

[71] G. Yue, J. Wu, Y. Xiao, M. Huang, J. Lin, L. Fan, Z. Lan, Platinum/graphene hybrid film as a counter electrode for dye-sensitized solar cells, Electrochim. Acta. 92 (2013) 64–70, http://dx.doi.org/10.1016/j.electacta.2012.11.020.

[72] D. Dahlan, S.K. Md Saad, A.U. Berli, A. Bajili, A.A. Umar, Synthesis of two-dimensional nanowall of Cu-Doped TiO_2 and its application as photoanode in DSSCs, Phys. E Low-Dimensional Syst. Nanostruct. 91 (2017) 185–189, http://dx.doi.org/10.1016/j.physe.2017.05.003.

[73] C. Wu, Y. Yue, X. Deng, W. Hua, Z. Gao, Investigation on the synergetic effect between anatase and rutile nanoparticles in gas-phase photocatalytic oxidations, Catal. Today 93–95 (2004) 863–869, http://dx.doi.org/10.1016/j.cattod.2004.06.087.

[74] G. Li, C.P. Richter, R.L. Milot, L. Cai, C.A. Schmuttenmaer, R.H. Crabtree, G.W. Brudvig, V.S. Batista, Synergistic effect between anatase and rutile TiO_2 nanoparticles in dye-sensitized solar cells, Dalt. Trans. (2009) 10078–10085, http://dx.doi.org/10.1039/b911129h.

[75] M.C. Kao, H.Z. Chen, S.L. Young, C.Y. Kung, C.C. Lin, The effects of the thickness of TiO_2 films on the performance of dye-sensitized solar cells, Thin Solid Films 517 (2009) 5096–5099, http://dx.doi.org/10.1016/j.tsf.2009.03.102.

[76] M. Fitra, I. Daut, M. Irwanto, N. Gomesh, Y.M. Irwan, Effect of TiO_2 thickness dye solar cell on charge generation, Energy Procedia 36 (2013) 278–286.

[77] A.Y. Ahmed Al-She'Irey, S.K. Md Saad, A.A. Umar, M.Y.A. Rahman, M.M. Salleh, (001) faceted-Ga- TiO_2 microtablet synthesis and its organic perovskite sensitized solar cells characterization, J. Alloys Compd. 674 (2016) 470–476, http://dx.doi.org/10.1016/j.jallcom.2016.02.270.

[78] L.H. Chang, C.K. Hsieh, M.C. Hsiao, J.C. Chiang, P.I. Liu, K.K. Ho, C.C.M. Ma, M.Y. Yen, M.C. Tsai, C.H. Tsai, A graphene-multi-walled carbon nanotube hybrid supported on fluorinated tin oxide as a counter electrode of dye-sensitized solar cells, J. Power Sources 222 (2013) 518–525, http://dx.doi.org/10.1016/j.jpowsour.2012.08.058.